


Single-Cell WGCNA Combined with Transcriptome Sequencing to Study the Molecular Mechanisms of Inflammation-Related Ferroptosis in Myocardial Ischemia-Reperfusion Injury

Zhuohua Zhang ^{1,2}, Yan Liu², Da Huang², Zhaohu Huang^{1,3,4}

¹Department of Cardiology, First Affiliated Hospital of Jinan University, Guangzhou, 510630, People's Republic of China; ²Department of Cardiology, Affiliated Hospital of Youjiang Medical University for Nationalities, Baise, 533000, People's Republic of China; ³Affiliated Southwest Hospital, Youjiang Medical University for Nationalities, Baise, 533000, People's Republic of China; ⁴Graduate School, Youjiang Medical University for Nationalities, Baise, 533000, People's Republic of China

Correspondence: Zhaohu Huang, Department of Cardiology, First Affiliated Hospital of Jinan University, Guangzhou, 510630, People's Republic of China, Tel +86 13977691455, Fax +86 776-2853272, Email bshuangzhaohu@163.com

Purpose: Myocardial ischemia-reperfusion injury (MIRI) is characterized by inflammation and ferroptosis, but the precise mechanisms remain unknown. This study used single-cell transcriptomics technology to investigate the changes in various cell subtypes during MIRI and the regulatory network of ferroptosis-related genes and immune infiltration.

Methods: Datasets GSE146285, GSE83472, GSE61592, and GSE160516 were obtained from Gene Expression Omnibus. Each cell subtype in the tissue samples was documented. The Seurat package was used for data preprocessing, standardization, and clustering. Cellphonedb was used to investigate the ligand-receptor interactions between cells. The hdWGCNA analysis was used to create a gene co-expression network. GSEA and GSEA were combined to perform functional enrichment and pathway analysis on the gene set. Furthermore, characteristic genes of the disease were identified using Lasso regression and SVM algorithms. Immune cell infiltration analysis was also performed. MIRI rat models were created, and samples were taken for RT-qPCR and Western blot validation.

Results: The proportion of MIRI samples in the C2, C6, and C11 subtypes was significantly higher than that of control samples. Three genes associated with ferroptosis (CD44, Cfl1, and Zfp36) were identified as MIRI core genes. The expression of these core genes was significantly correlated with mast cells and monocyte immune infiltrating cells. The experimental validation confirmed the upregulation of Cd44 and Zfp36 expression levels in MIRI, consistent with current study trends.

Conclusion: This study used single-cell transcriptomics technology to investigate the molecular mechanisms underpinning MIRI. Numerous important cell subtypes, gene regulatory networks, and disease-associated immune infiltration were also discovered. These findings provide new information and potential therapeutic targets for MIRI diagnosis and treatment.

Keywords: myocardial ischemia-reperfusion injury, ferroptosis, immune cell infiltration, single-cell transcriptome sequencing, WGCNA

Introduction

Patients who develop an acute myocardial infarction and are unable to receive early percutaneous coronary intervention (PCI) have a higher risk of death.¹ Until now, PCI and coronary artery bypass grafting have been critical approaches to alleviating coronary artery obstruction.^{2,3} Numerous studies have shown that restoring coronary blood flow after obstruction can cause myocardial ischemia-reperfusion injury (MIRI),⁴ which is characterized by cell death and inflammation.⁵ Thus, it is critical to investigate the underlying therapeutic targets for MIRI. Researchers have extensively researched cell death, an essential aspect of MIRI. Ferroptosis has been linked to a wide range of pathological events, including renal degeneration, tissue damage, cancer, and stroke.⁶

Ferroptosis is a unique type of iron-dependent, non-apoptotic cell death. Mitochondria are primarily characterized by morphological changes, such as decreased mitochondrial volume, increased and ruptured mitochondrial membrane density, and reduced or absent mitochondrial cristae. These changes differ significantly from mitochondrial changes in apoptosis, necrosis, autophagy, and other mechanisms. The biochemical changes primarily manifest as the cell deposits copious amounts of iron and lethal reactive oxygen species and the depletion of endogenous iron death inhibitors such as reduced glutathione, glutathione peroxidase 4, and vitamin E.⁶ Studies have shown that Ferroptosis activators activate this process and exacerbate MIRI.^{7,8}

Apart from that, ferroptosis inhibitors are protective in MIRI mitigation.⁹ It is critical to emphasize the importance of ferroptosis in MIRI. Despite this, there has been no significant progress in developing ferroptosis-related drugs for clinical use. Furthermore, there is little research on the effects of approved drugs on ferroptosis. Thus, further research is needed to thoroughly investigate the pathogenesis and potential therapeutic targets of ferroptosis in MIRI.

Bioinformatics analysis has become an increasingly popular tool for identifying key genes and performing subsequent analyses with high efficiency and specificity. While bulk RNA sequencing can only estimate average gene expression in a cell population, the recent advancement of single-cell RNAseq enables the discovery of specific information and correlations at a higher resolution, focusing on individual cells.^{10,11} This study aims to identify potential therapeutic targets by investigating key genes associated with ferroptosis in MIRI using a single-cell cooperative transcriptomics approach.

Data Set Source

1. scRNA Data set (GSE146285).
2. RNA-seq dataset (GSE83472, GSE61592, GSE160516).

Materials and Methods

Data Download

The Gene Expression Omnibus (GEO) database (<https://www.ncbi.nlm.nih.gov/geo/info/datasets.html>), managed by the US National Center for Biotechnology Information (NCBI), is a repository for gene expression data. GSE146285 yielded 31 samples for single-cell analysis. The GSE83472 Series Matrix File and the GPL6885 annotation file contained expression profile data from eight individuals: four from the control group and four from the disease group. Similarly, GSE61592 presented expression profile data from six individuals, three from each group, using the Series Matrix File and annotated file GPL6887. The GSE160516 Series Matrix File was downloaded from the NCBI GEO public database, with GPL23038 as the annotated file. Finally, GSE160516 included data from 16 patients: 4 in the control and 12 in the experimental group. This information was gathered using the Series Matrix File and annotated file GPL23038.

Single-Cell Analysis

The Seurat package¹² was used to analyze the expression profile. Low-expression genes (%mt < 20) were then screened out. The data underwent standardization, homogenization, PCA, and harmony. The ideal number of principal components was determined using an elbow plot, and the spatial relationship of each cluster was visualized using uniform manifold approximation and projection (UMAP) analysis.

Analysis of Interaction Between Ligand Receptors

The EDB Cell Phone tool (Cellphonedb)¹³ enables the quantitative analysis and inference of intercellular communication networks using data from individual cells. Cellphonedb predicted the primary cell signal inputs and outputs using pattern recognition and network analysis methods and evaluated how these signals control cell functions. Using standardized single-cell expression profiles as input data, this study identified cell subtypes from single-cell analysis, providing specific information about each cell. The focus was on cell interactions to assess their frequency and intensity. It was done to determine the proximity of the interactions and the effect of each cell type on the disease context.

Analysis of hdWGCNA

The hdWGCNA software package¹⁴ included gene module identification, network inference, functional gene enrichment analysis, statistical testing for network reproducibility, and data visualization. In addition to conventional single-cell RNAseq, it could perform homotypic network analysis on long-read single-cell data. The Setup For WGCNA method was used to build a co-expression network of genes expressed in at least 5% of the cells in Seurat objects, with a soft threshold of 12. The WGCNA tree was displayed using PlotDendrogram, a popular visualization technique for displaying the core presentation modules generated by network analysis. A leaf on the tree represented each gene, and the color at the base indicated the categorization of co-expression modules. Finally, GetMEs was used to display the MEs level for each module.

Gene Function Enrichment Analysis

The Metascape database (<https://www.metascape.org>) was utilized to functionally annotate genes associated with key modules to investigate their functional relationships thoroughly. Individual genes underwent pathway analysis using Gene Ontology (GO), with a minimum overlap of three or more and a statistically significant p-value of less than or equal to 0.01.

Feature Selection Using Lasso Regression and SVM Algorithm

SVM and Lasso logistic regression algorithms were used to select disease diagnostic markers. The “glmnet” software package¹⁵ was used to implement the Lasso algorithm. Additionally, a machine learning technique, SVM-RFE, based on support vector machines, was used to identify optimal variables by removing feature vectors generated by SVM. Subsequently, a model based on support vector machines was created using the “e1071” software package to assess the diagnostic utility of these biomarkers in diseases.

Evaluation of Immune Cell Infiltration

The CIBERSORT technique¹⁶ accurately classified immune cells in the microenvironment. The expression matrix of various immune cell subtypes was analyzed using deconvolution principles based on support vector regression. This technique differentiates between 25 immune cell phenotypes in mice using a set of 547 biomarkers. This study analyzed the sample data using the CIBERSORT algorithm to estimate the proportional distribution of the 25 different types of immune infiltrating cells. Additionally, a Pearson correlation analysis investigated the relationship between immune cell composition and gene expression.

Gene Set Variation Analysis

This study used GSVA to assess gene set enrichment in transcriptome data. In terms of GSVA, it scored the entire gene set while translating individual gene expression shifts into pathway-level changes. This method generated holistic scores for each gene set, allowing for the assessment of a sample’s biological functions. Using the GSVA algorithm, this study obtained gene sets from the Molecular Signatures Database and investigated underlying biological functional shifts across different samples. At the same time, this approach provided a powerful tool for investigating gene expression modes and understanding the hidden biological processes in a sample.

GSEA Analysis

Patients were divided into two groups based on their gene expression levels: high and low. Aside from that, GSEA was used to compare these groups’ signaling pathways. Moreover, this study relied on annotated gene sets from version 7.0 (<https://www.gsea-msigdb.org/gsea/msigdb>) as a foundation for subtype pathways. The differential expression of the pathway between subtypes was investigated. Sequencing was limited to gene sets that were significantly enriched (adjusted p-value < 0.05). Generally speaking, GSEA analysis investigates the complex relationship between biological significance and disease classification. The GSEA analysis revealed significant differences in signaling pathways between patients’ low- and high-expression groups. At the same time, annotated gene sets were used, and pathway differential expression analysis was performed to identify the significant enrichment of gene sets, which suggested implications for

biological relevance and disease classification. This method clarified the relationships between gene expression levels and signaling pathways and expands on the potential mechanisms underlying disease subtypes. Moreover, GSEA analysis is a powerful tool for understanding the complex interaction of disease features and genetic expression patterns.

Analysis of Regulatory Networks of Key Genes

Transcription factors were predicted using motif analysis with the R package “RcisTarget”. The analysis of motifs served as the foundation for predicting transcription factors. Additionally, a motif’s normalized enrichment score (NES) is calculated using the number of motifs. Furthermore, additional annotation files were created by inferring motifs from genetic sequences and identifying similarities. The first step was computing the area under the curve (AUC) for each pair of motifs to determine the impact of motif overexpression on gene sets. The recovery curve of genetic sequences determined the AUC within the gene set. Finally, the NES for each motif was determined by examining the distribution of AUC across all motifs in the gene set.

Construction of miRNA Network

MicroRNAs (miRNAs) are tiny non-coding RNAs regulating gene expression by promoting mRNA degradation or inhibiting mRNA translation. This study focused on identifying miRNAs that target critical genes that regulate or degrade harmful genes. The TargetScan database was used to identify miRNAs associated with core genes, and Cytoscape software was used to visualize the gene-miRNA network.

MIRI Model

Collection of Samples

Sixteen adult male Sprague-Dawley rats, having a weight ranging from 220 to 250 grams, were obtained from Changsha Tianqin Biotechnology Co., Ltd. [License No.: scxk (Xiang) 2022–0011]. All rats were accommodated under thermoregulated circumstances with a 12-hour light-dark cycle and had unrestricted access to food and water.

MIRI Protocol

Rats were given an intraperitoneal injection of 1% pentobarbital (40 mg/kg) and placed in a supine position for anesthesia. The trachea was then separated via a neck incision and attached to a miniature artificial respirator. Electrodes were placed beneath the limbs to monitor the electrocardiogram. A midline incision was made through the skin and sternum of the rat’s chest to expose the heart. The left anterior descending branch of the coronary artery was identified and ligated with a medical suture. After 45 minutes, reperfusion was performed for an additional 30 minutes. The subsequent electrocardiogram revealed ventricular premature contractions, ventricular tachycardia, ventricular fibrillation, and other reperfusion arrhythmias. Elevated ST segment descent and T-wave recovery indicated successful reperfusion. Rats were randomly chosen and divided into two groups: one group underwent sham surgery, and the other served as the model, each containing eight rats. The model group created the MIRI model using the previously mentioned method, whereas the sham surgery group had threading done without ligation. The animal experimentation facility is located in the animal operating room of the Affiliated Hospital of Youjiang Medical College for Nationalities. The study was approved by the Research Ethics Committee of the Affiliated Hospital of Youjiang Medical College of Nationalities (ethics approval number: YYFY-LL-2024-029).

Assessment of Myocardial Infarct Size

Myocardial tissues collected from rats following IR were rinsed in pre-cooled saline and then cut into 1 mm sections. These sections were immersed in a 2% solution of triphenyltetrazolium chloride (TTC, league, China) for 15 minutes in a dark water bath at 37 °C. Subsequently, the sections were fixed in 10% methanol overnight before being examined under a microscope. Myocardial infarction tissues appeared white due to dehydrogenase loss, whereas normal myocardial tissues were red due to dehydrogenase-mediated TTC reduction. The stained section was imaged with a digital camera, and the white infarct region of the anterior section was analyzed via ImageJ, divided by the total area of the section, and presented as a percentage.

Organizational Pathological Changes

Hematoxylin-eosin (H&E) staining was utilized to evaluate the pathological and morphological changes of myocardial tissue. The hearts of each group were fixed overnight in 4% paraformaldehyde, then dehydrated and embedded in paraffin blocks. The myocardial tissues were then sectioned into 5%-thick slices, mounted on glass slides, dried, and stained. A light microscope was utilized to inspect paraffin-embedded myocardial tissue slices which were stained with hematoxylin for 5 minutes and eosin for 2 minutes. (Beijing Sola Biotechnology Co., Ltd., China). Finally, the stained slides were deparaffinized in xylene and dehydrated using gradient concentrations of ethanol as directed before being sealed with resin.

Measurement of cTnT and CK-MB

Myocardial injury was assessed by measuring lactate dehydrogenase (LDH) and creatine kinase (CK-MB) plasma levels. At the end of the reperfusion period, blood was collected and centrifuged at 1500 rpm for 10 minutes to extract plasma. LDH and CKMB levels and activity were determined using specific ELISA kits (Nanjing Jiancheng Bioengineering Research Institute) according to the manufacturer's protocols.

Reverse Transcription – Quantitative PCR (RT-qPCR)

Total RNA was extracted from rat myocardial tissue using the Trizol method. Subsequently, an appropriate amount of RNA was utilized to synthesize cDNA via reverse transcription. A 10 μ L reaction system was prepared with a PCR kit under the following conditions: initial denaturation at 95 °C for 10 minutes, followed by 40 PCR cycles (95 °C for 10 seconds, 55 °C for 20 seconds, and 72 °C for 15 seconds). The relative expression levels of Cd44, Zfp36, and Cfl1 in the tissue were determined using the $2^{-\Delta\Delta Ct}$ method. The relative expression levels of Cd44, Zfp36, and Cfl1 in the tissue were determined using the $2^{-\Delta\Delta Ct}$ method. [Table S1](#) includes primer sequences for Cd44, Zfp36, Cfl1, and the reference gene β -actin.

Western Blot Analysis

Total protein was extracted from infarcted tissue in the rat's left ventricular using RIPA lysis buffer (Solarbio, China) and PMSF. A BCA protein assay was used to determine protein content, and protein samples were subjected to electrophoretic separation on SDS-PAGE prior to their translocation onto a polyvinylidene difluoride membrane. After a 2-hour blocking stage with 5% skim milk, the membranes were incubated overnight at 4 °C with the primary antibody at a dilution factor of 1:1,000. In the wake of a wash with PBS containing 0.2% Tween, the membrane was incubated with a secondary antibody for 1 hour at room temperature. The signals were subsequently detected by means of Pierce's ECL Western Blotting Substrate. The intensity of the bands was quantified through the utilization of Image J software and normalized to GAPDH. The antibodies directed towards Cd44 (ab316123), Caspase3 (ab184787), and Bcl2 (ab203516) were obtained from Abcam (San Francisco, CA), whereas Zfp36 (MG202381S) was procured from Abmart (Shanghai Co., Ltd).

Statistical Analysis

This study used R language (version 4.3.0) for analysis. All statistical analyses were performed as two-tailed tests, with a significance level established at $p < 0.05$.

Results

Initial Data Preparation for Single-Cell Gene Expression Profiles

The analysis used expression profiles from tissue samples from 31 MIRI cases. Only cells with expression profiles less than 20% mt were considered for analysis, yielding 9,365 cells with feature expression levels for further investigation ([Figure 1A](#) and [B](#)). [Figure 1C](#) shows the top ten genes with the highest standard deviation. Principal component analysis (PCA) revealed batch effects in the samples. This resulted in the application of harmonic analysis for dimensionality reduction and batch correction ([Figure 1D](#)). Subsequently, UAMP identified 21 subtypes ([Figure 2A](#)).

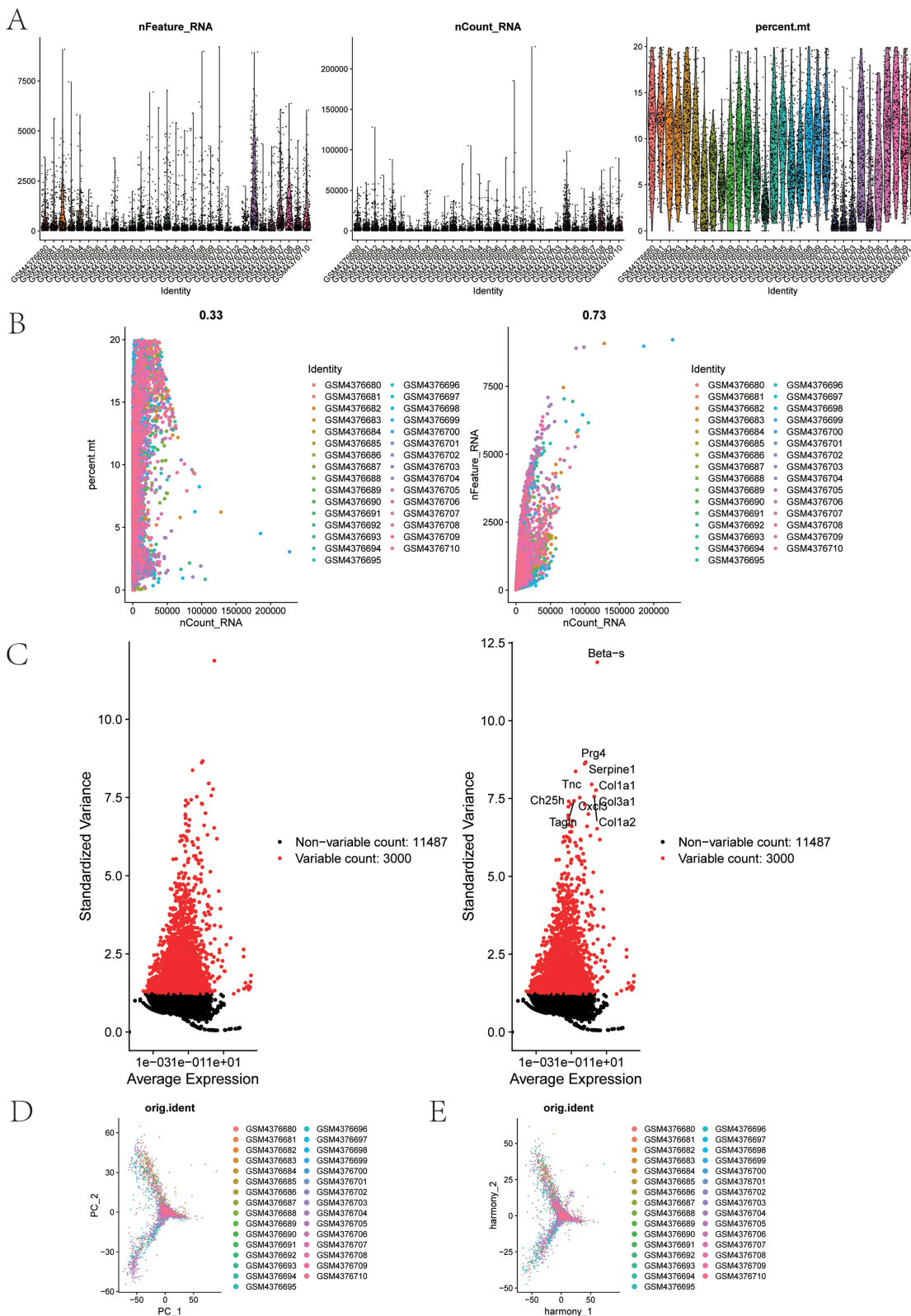


Figure 1 Single-cell pre-processing. **(A)** Single cell quality control includes the number of cells, number of genes, and sequencing depth of each sample. **(B)** The left plot shows the relationship between cell sequencing depth and mitochondrial content, while the right plot shows the relationship between sequencing depth and gene number, both showing a positive correlation. **(C)** Genes that significantly differed between cells were identified and their characteristic variance was plotted. **(D and E)** Principal component analysis (PCA) display and PC distribution, where dots represent cells and colors represent samples.

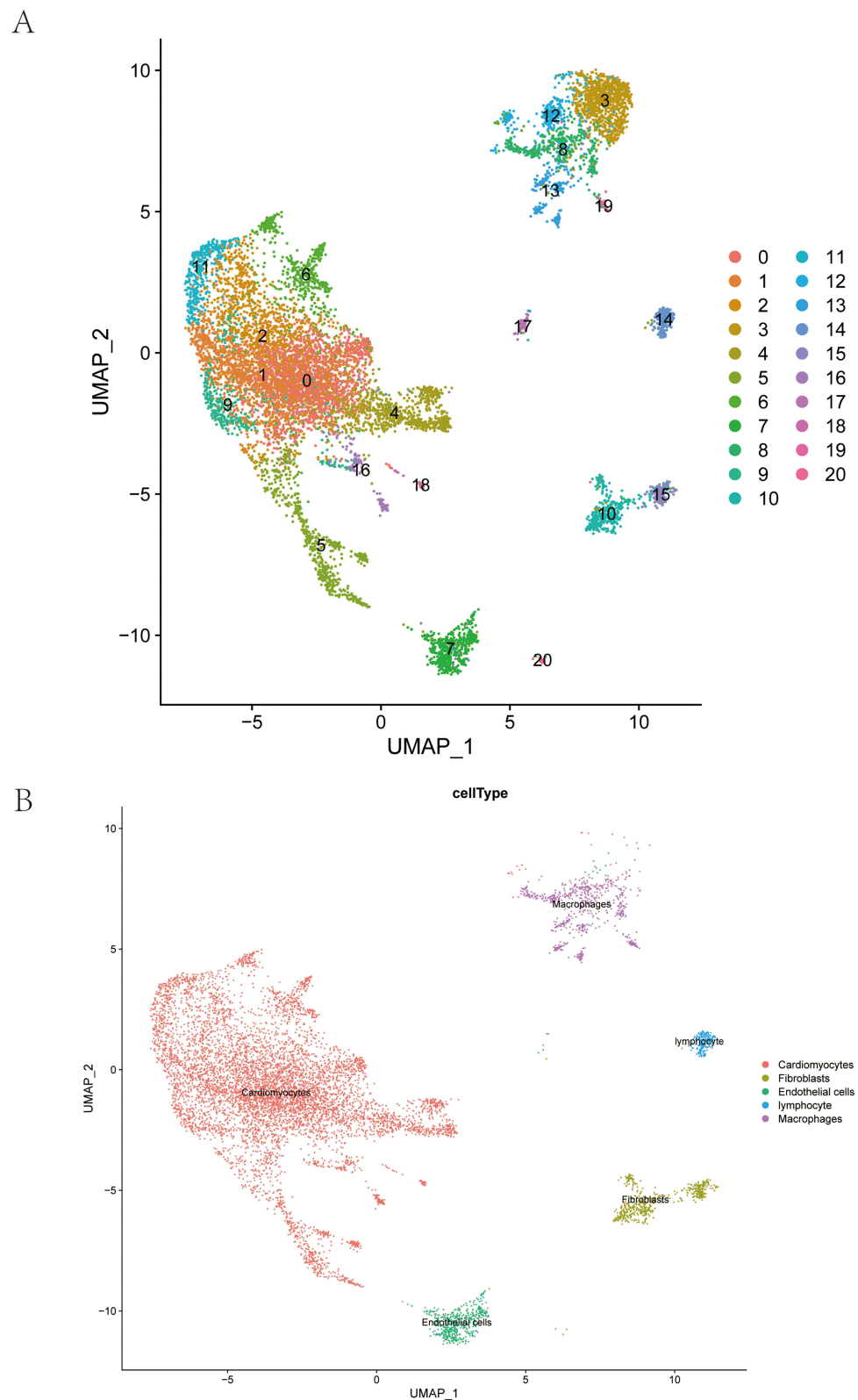


Figure 2 Annotation of cells. **(A)** We divided the cells into 21 clusters through the UMAP algorithm according to the important components available in PCA. **(B)** Cell annotation of 21 clusters. 21 clusters are annotated into 5 cell types, namely Cardiomyocytes, Fibroblasts, Endothelial cells, Lymphocytes, and Macrophages.

Annotation of Cluster Subtypes and Analysis of Receptor-Ligand Relationship Pairs

Each subtype was annotated using the R package SingleR, resulting in 21 clusters classified as cardiomyocytes, fibroblasts, endothelial cells, lymphocytes, and macrophages (Figure 2B). Cardiomyocyte subtypes were further analyzed with PCA, Harmony, and FindClusters, yielding 12 subtypes (Figure 3A–C). Subtypes C2, C6, and C11 had a higher prevalence of disease samples than the others (Figure 3D). Furthermore, the cell chart tool examined the interactions between ligands and receptors in single-cell gene expression data, revealing complex pairs of interactions between these cellular subgroups (Figure 3E and F).

Analysis of hdWGCNA

This study determined the coexpression network of genes in the cardiomy subtype using hdWGCNA analysis. The data were categorized based on the clustering findings after secondary clustering of cardiomyocytes to form a coexpression network and further investigate potential biomarkers during disease progression. The soft threshold of 12 was determined using the “TestSoftPowers” function (Figure 4A). The analysis revealed four gene modules: yellow, turquoise, brown, and blue (Figure 4B). Further investigation of the relationship between modules and ME levels (Figure 4C and D) revealed that the brown module had higher ME levels than the disease cell subtypes (Figure 4E). As a result, 84 genes from the brown module were chosen as candidates for future studies (Table S2).

Functional Enrichment of Module Genes and PCA Correction

Further analysis of the brown module gene’s pathway revealed enrichment in neutrophil chemotaxis, positive regulation of cell motility, and response to type II interferon, among other pathways (Figure 5A). Datasets from GSE83472, GSE61592, and GSE160516 were obtained from the GEO database and included the expression profiles of 30 patients, 11 in the control group and 19 in the disease group. The SVA algorithm was used to correct chip-related variations, and PCA diagrams showed the batch conditions before and after correction. The results showed that applying the SVA algorithm for correction reduced batch effects across chips (Figure 5B and C).

Identification of Crucial Genes and Their Expressions in Individual Cell Datasets

The GeneCards database (<https://www.genecards.org/>) was searched for genes involved in ferroptosis progression and potential genes from the brown module to identify essential genes influencing MIRI. We identified 19 common genes using an intersection analysis (Figure 6A). We then used Lasso regression and the SVM algorithm to identify characteristic genes associated with MIRI. Lasso regression identified five genes as significant for this condition (Figure 6B and C). Similarly, SVM algorithm analysis revealed the top seven feature genes with the lowest error rate in the MIRI dataset (Figure 6D). By intersecting these genes with those identified by Lasso regression, we discovered Cd44, Cfl1, and Zfp36 as hub genes for further investigation (Figure 6E). The expression levels of Cd44 ($r = -0.488$), Zfp36 ($r = -0.537$), and Cfl1 ($r = -0.466$) were all negatively correlated with Gpx4 (Figure 6F–H).

These three hub genes are the focus of this study, with expressions in five different cell types being investigated (Figure 7A–C).

Analysis of Immune Infiltration

The microenvironment is primarily composed of immune cells, an extracellular matrix, various growth and inflammatory factors, and distinct physical and chemical characteristics, all of which significantly impact disease diagnosis and clinical treatment effectiveness. This study investigated the potential molecular mechanisms by which key genes influence the progression of myocardial injury caused by ischemia and reperfusion. It was accomplished by investigating the correlations between potential genes and immune cell infiltration in the MIRI dataset. It displays the proportion of immune cells in each patient and the relationship between immune cells in various forms in Figure 8A and B. At the same time, it discovered that DC Activated, DC Immature, Eosinophil Cells, M0 Macrophage, M2 Macrophage, Mast Cells, Monocyte, T Cells CD4 Memory, T Cells CD8 Memory, and T Cells CD8 Naive were significantly different between the two groups (Figure 8C). This study further explored the relationship between key genes and immune cells. Cfl1 correlated significantly positively with T cells CD8 Naive and Monocytes but negatively with Mast Cells and T Cells CD8 Memory (Figure 8E). Cfl1

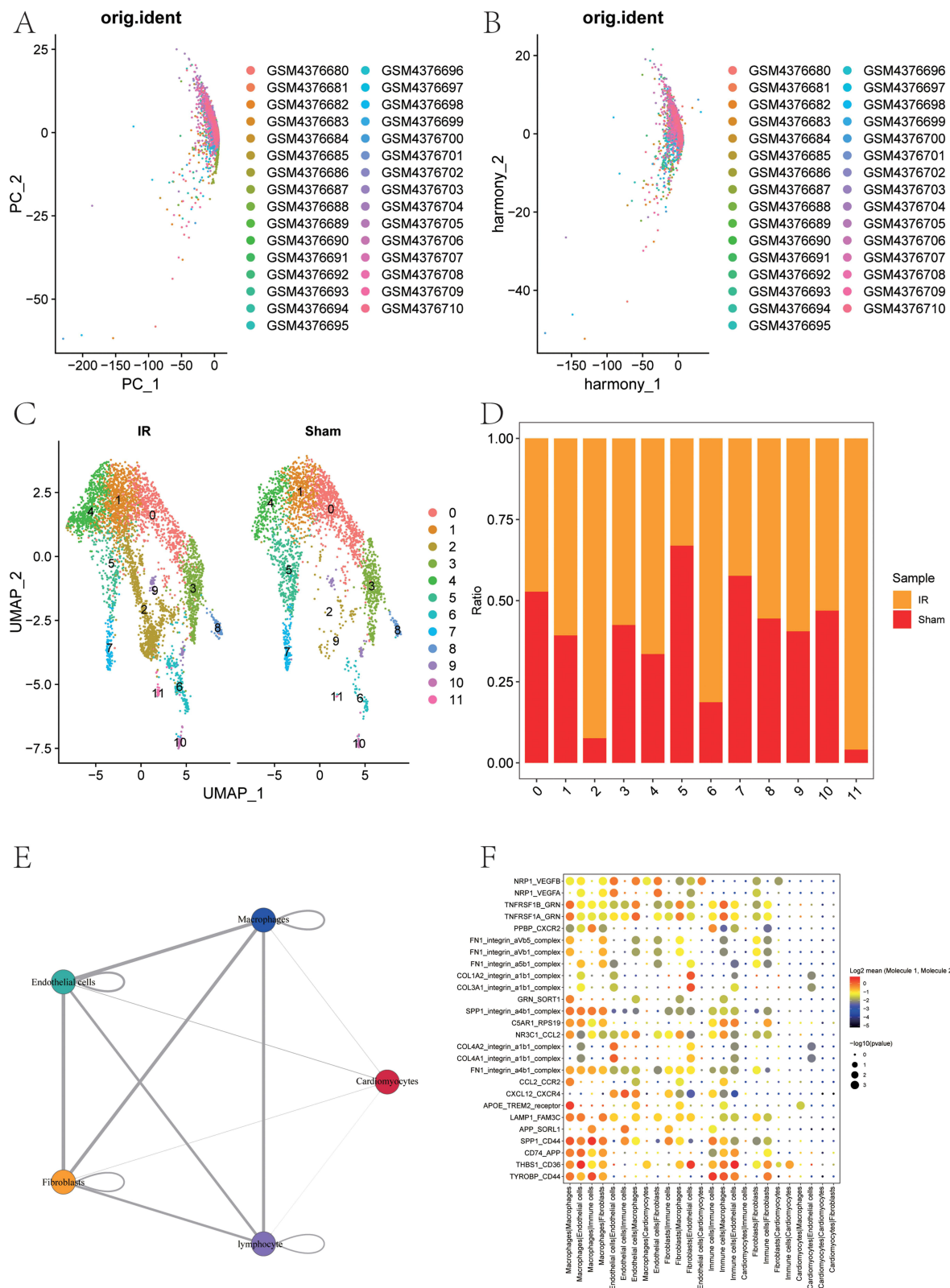


Figure 3 Display of secondary clustering PCA of cardiomyocytes. (**A** and **B**) and the distribution of PCs. The dots represent cells and the colors represent samples. (**C**) We divided the cells into 12 clusters through the UMAP algorithm based on the important components available in PCA. (**D**) The difference in the proportion of 12 types of cells in the two groups of samples. (**E**) Cellular interaction network among five types of cells. (**F**) Bubble plot of receptor ligands from cell to cell.

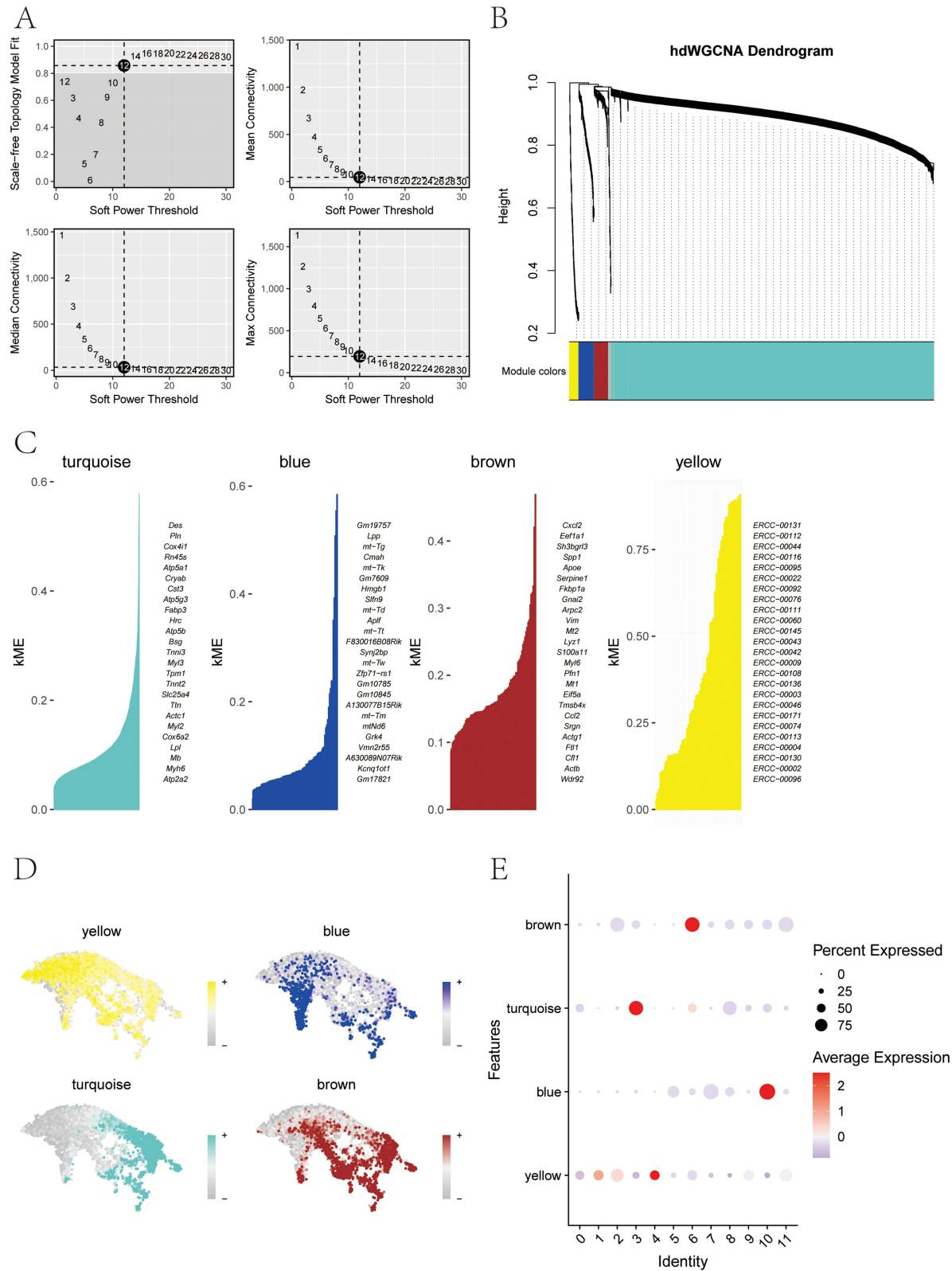


Figure 4 Single-cell WGCNA. **(A)** Scale-free index and average connectivity for each soft threshold. **(B)** Dendrogram of gene clustering, with different colors representing different modules. **(C and D)** Feature maps of top-ranked feature genes of different modules and module scores. **(E)** Correlation between module signature genes.

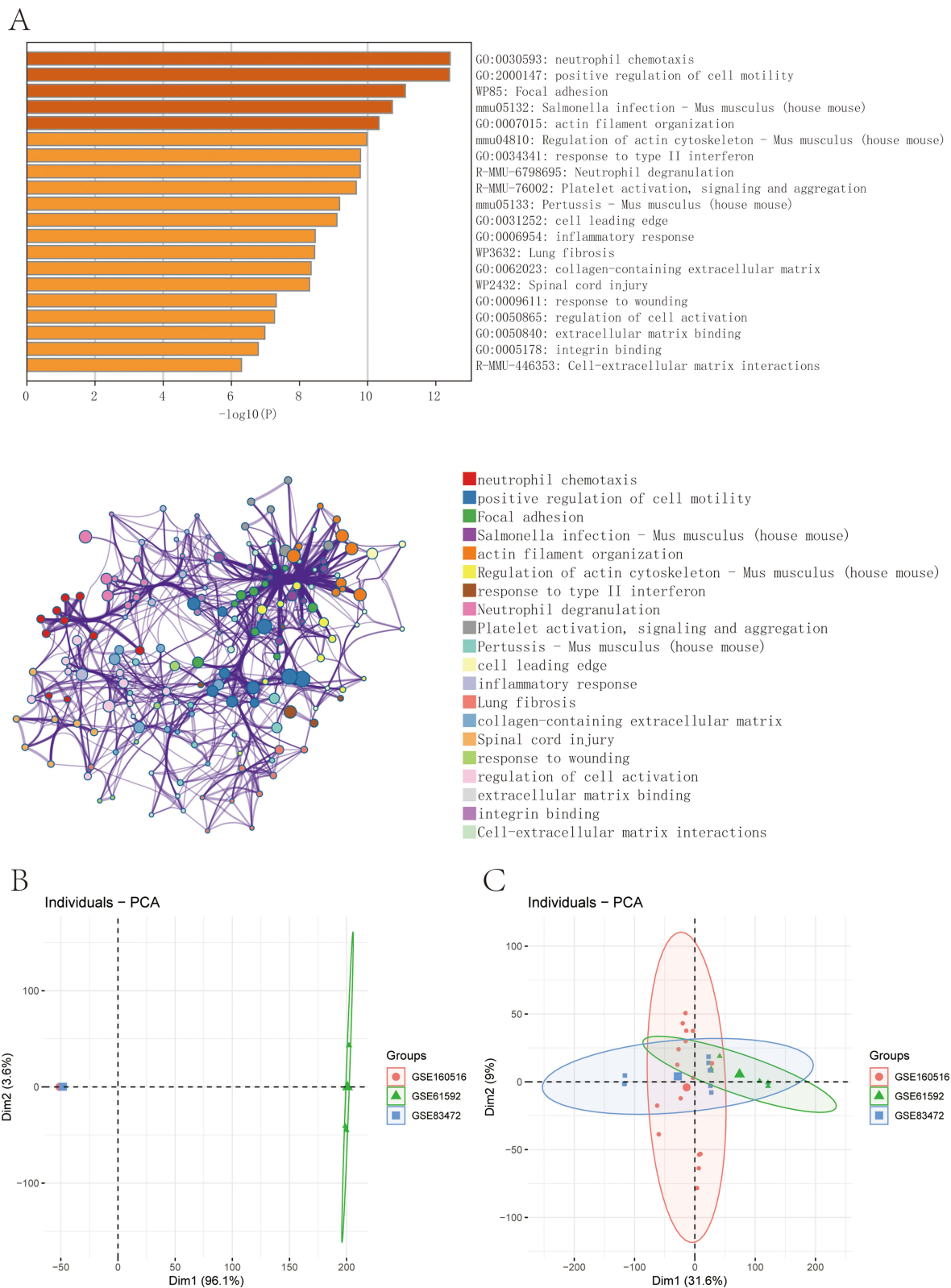


Figure 5 Enrichment analysis and batch effect. **(A)** Enrichment analysis using Metascape database GO-KEGG. **(B and C)** Batch effect before and after correction.

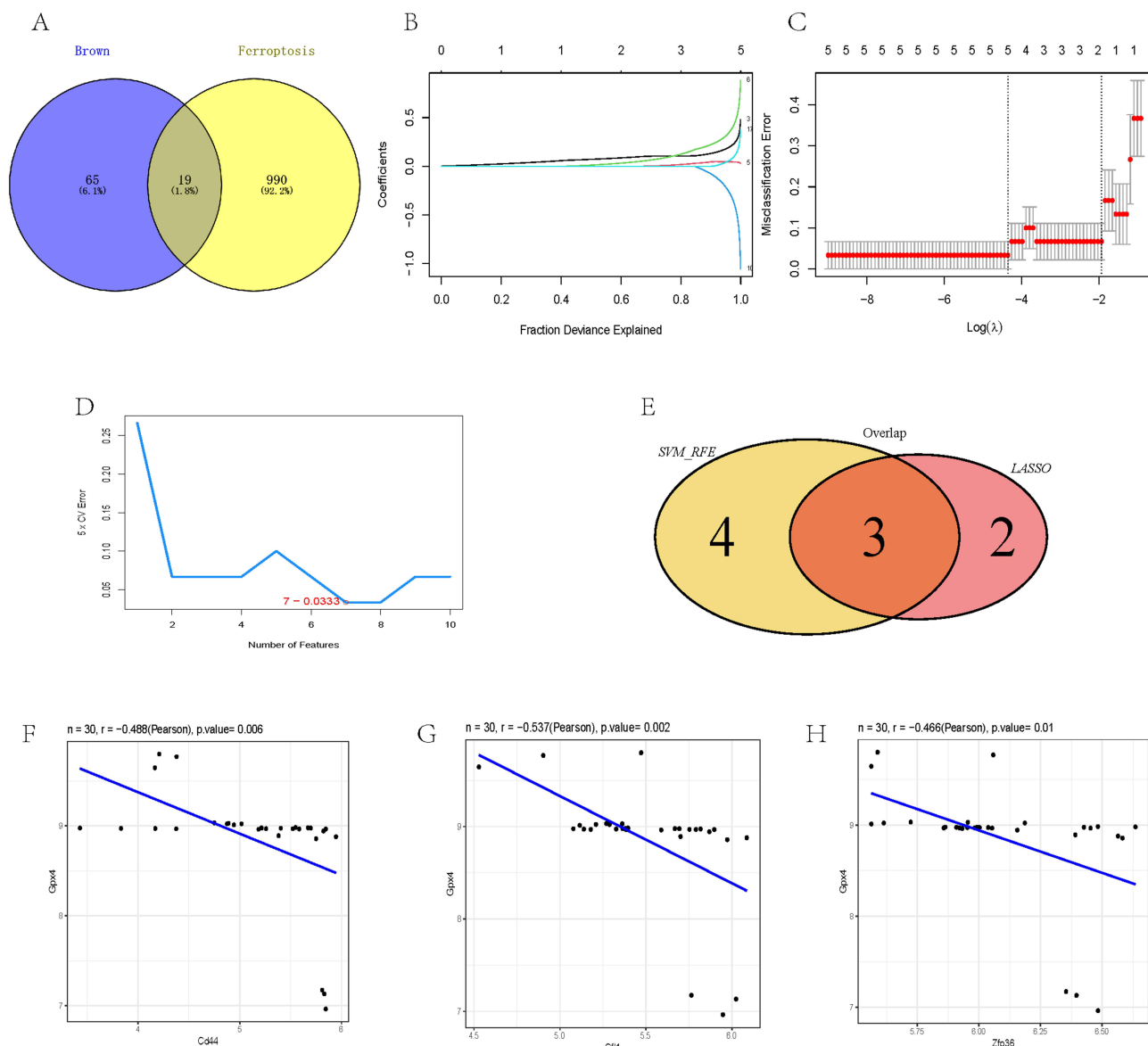


Figure 6 Construction of Lasso model. **(A)** Venn diagram of the intersection of brown module and ferroptosis gene. **(B)** LASSO coefficient distribution and gene combination at minimum lambda value. **(C)** Ten-fold cross-validation of tuning parameter selection in the LASSO model to determine the minimum lambda value. **(D)** The top 7 characteristic genes with the lowest error rate. **(E)** The intersection of the characteristic genes selected by the Lasso regression algorithm and the SVM algorithm. The Pearson correlation analysis demonstrated that Cd44, Zfp36, and Cfl1 exhibited a negative correlation with Gpx4 **(F–H)**.

correlated significantly positively with T cells CD8 Naive and Monocytes but negatively with Mast Cells and T Cells CD8 Memory (Figure 8E). Figure 8F shows significant positive correlations between Zfp36 and DC Activated and Monocyte cells. In contrast, significant negative correlations were observed between Zfp36 and DC Immature and Mast Cells. Next, this study analyzed the relationship between the three essential genes and various immune components from the TISIDB database. It included immune modulators, cytokines, and cellular surface proteins (Figure 9A–E). The findings show a strong link between these key genes and the extent of immune cell penetration, emphasizing their importance in shaping the immune environment.

Pathway Enrichment Analysis of Key Genes

Investigating the specific signaling pathways associated with the three key genes sought to elucidate the potential molecular mechanisms by which these genes influence disease progression. The GSVA results revealed a link between elevated Cd44 levels and the enrichment of the IL6_JAK_STAT3_SIGNALING and IL2_STAT5_SIGNALING pathways (Figure 10A). Similarly, Figure 10B shows that increased Cfl1 levels enhanced the PI3K_AKT_MTOR_SIGNALING and P53_PATHWAY pathways

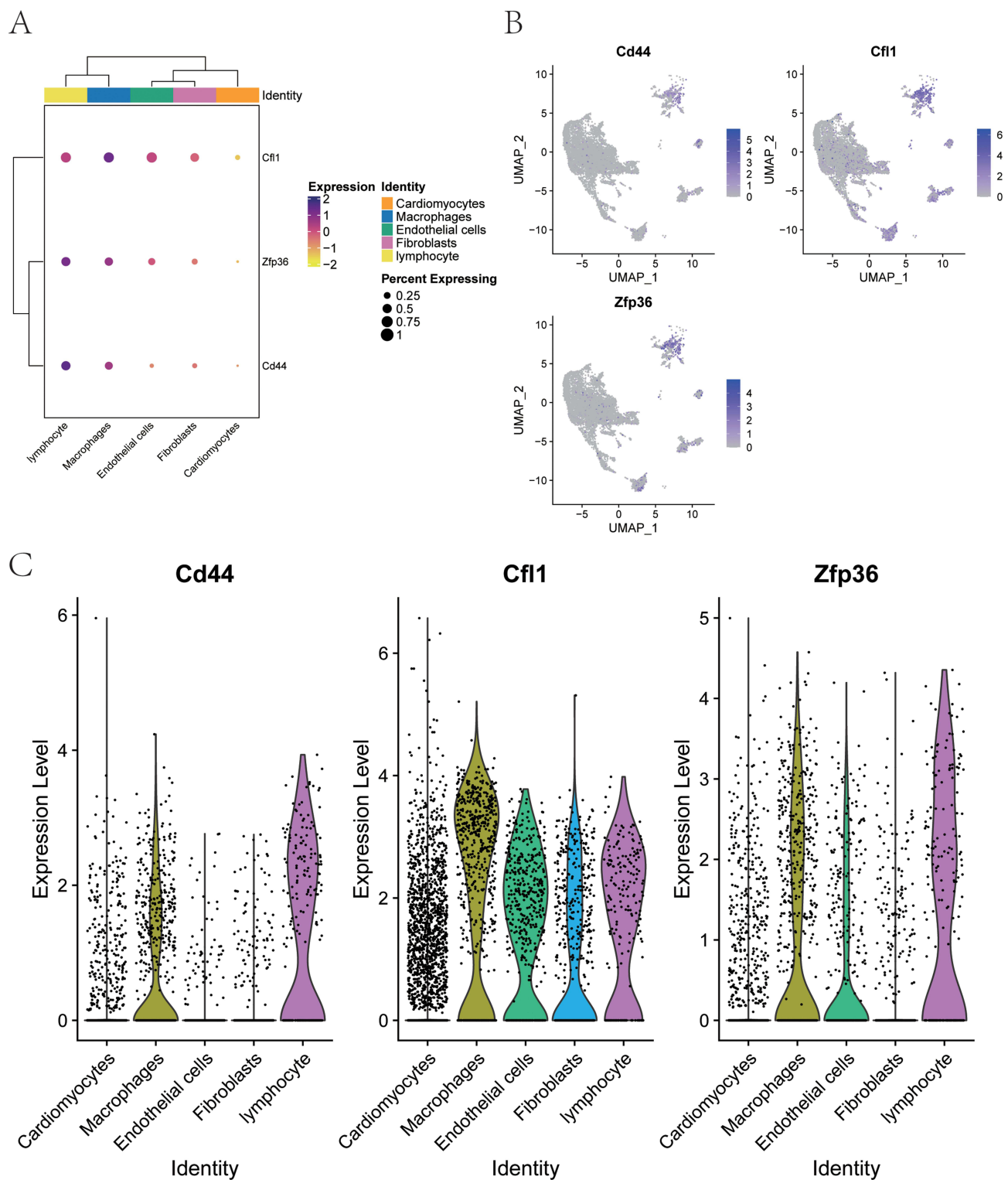


Figure 7 Single cell expression profile of key genes in cells (A–C).

(Figure 10B), whereas high Zfp36 expression enriched TGF_BETA_SIGNALING, MTORC1_SIGNALING, and other pathways (Figure 10C). GSEA results showed that Cd44 was involved in several pathways, including DNA synthesis, the TNF signaling pathway, and the IL-17 signaling pathway (Figure 11A and B). Cfl1 was abundant in pathways such as the cytosolic DNA sensing pathway, the Toll-like receptor signaling pathway, and the NF-kappa B signaling pathway (Figure 11C and D).

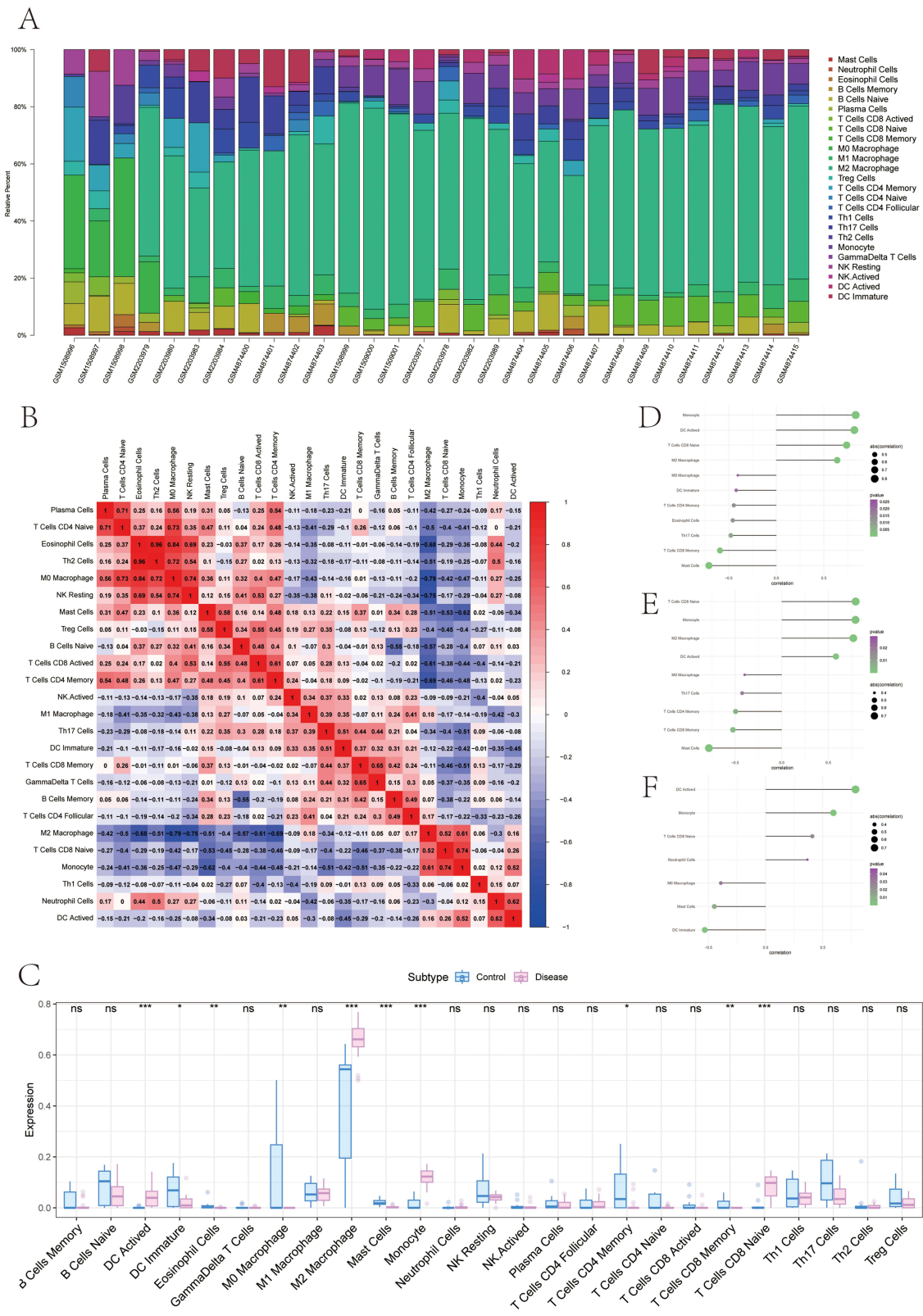


Figure 8 Immune infiltration (A) Relative percentages of 25 immune cell subpopulations in patients in the control group and disease group. (B) Pearson correlation between 25 types of immune cells, blue indicates negative correlation and red indicates positive correlation. (C) The difference in immune cell content between patients in the control group and the disease group. Blue indicates patients in the control group and pink indicates patients in the disease group. * $P < 0.05$ vs SHAM group, ** $P < 0.01$ vs SHAM group, *** $P < 0.001$ vs SHAM group. (D–F) Correlation between key genes and immune cell content. * $P < 0.05$ vs SHAM group, ** $P < 0.01$ vs SHAM group, *** $P < 0.001$ vs SHAM group.

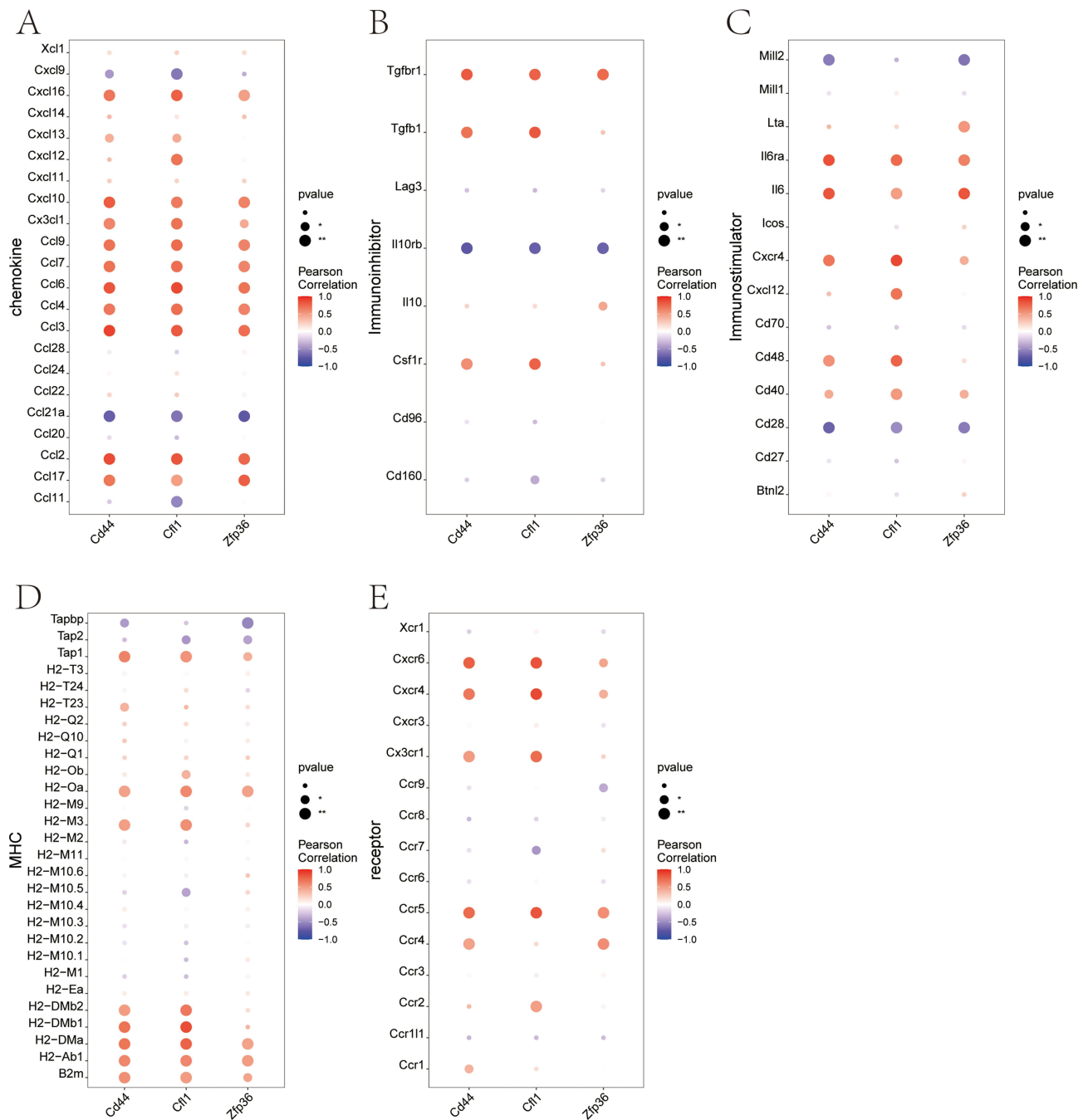


Figure 9 Correlation between key genes and immune factors. Correlation of key genes with chemokine, Immunoinhibitor, Immunostimulator, MHC and receptor (A–E).

Zfp36, on the other hand, was linked to pathways such as the B cell receptor, chemokine, and C-type lectin receptor (Figure 11E and F). These findings suggest adjusting these pathways could influence disease progression via the primary genes.

Transcriptional Regulation Analysis of Key Genes

This study analyzed three key genes in a gene cluster and discovered that they are controlled by shared mechanisms involving various transcription factors. The cumulative recovery curves revealed an enrichment of these transcription factors. The motif transfac_pro_M05673 had the highest standardized enrichment score (NES: 9.36). The enriched motifs of key genes and their corresponding transcription factors are shown in Figure 12A and B.

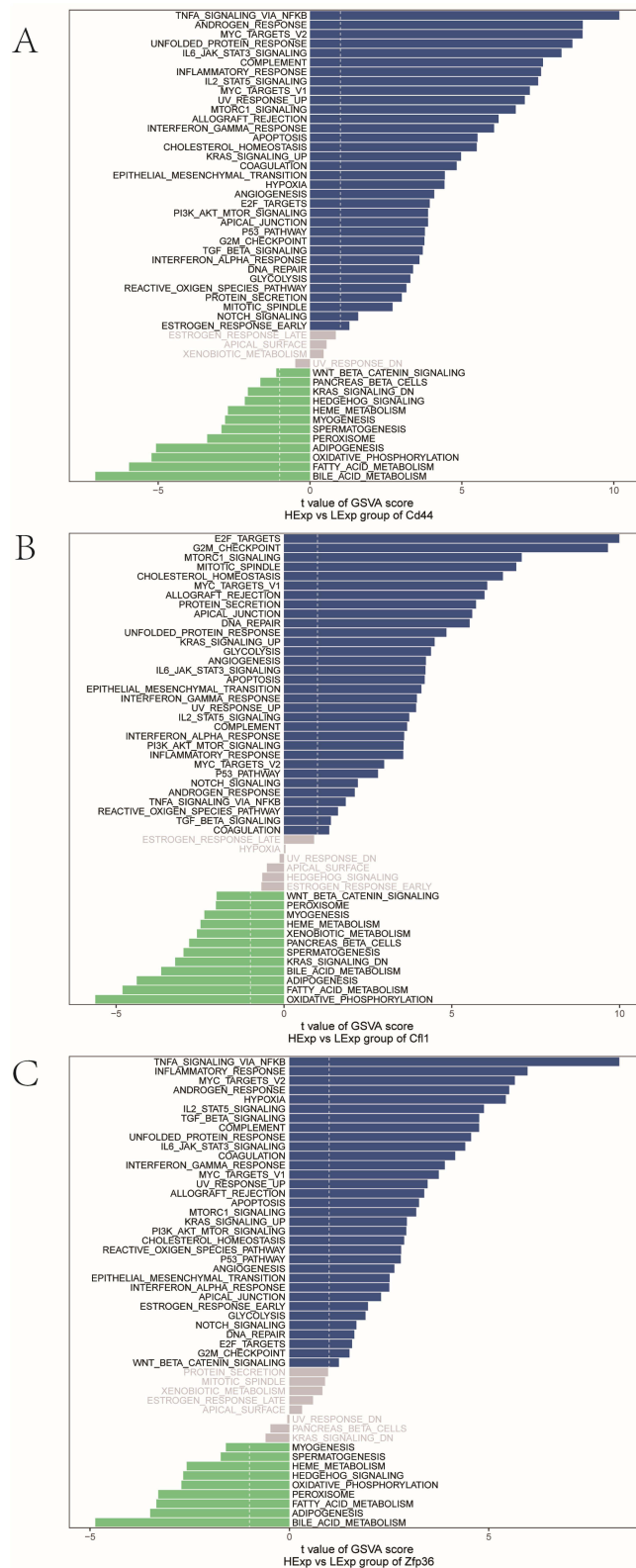


Figure 10 GSVA analysis of key genes. Blue indicates the signaling pathways involved in high-expression genes, green indicates the signaling pathways involved in low-expression genes, and the background gene set is the hallmark (A–C).

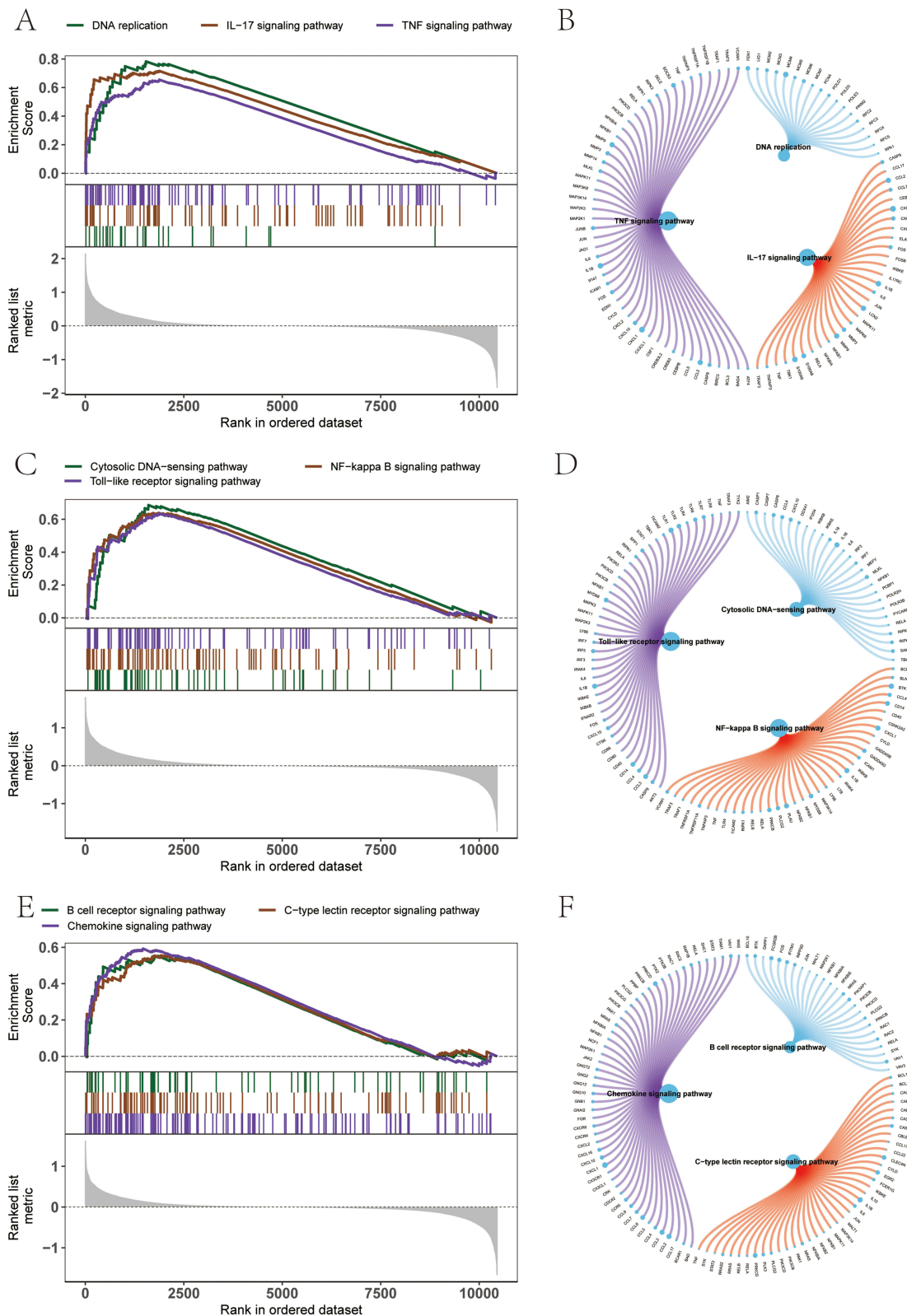
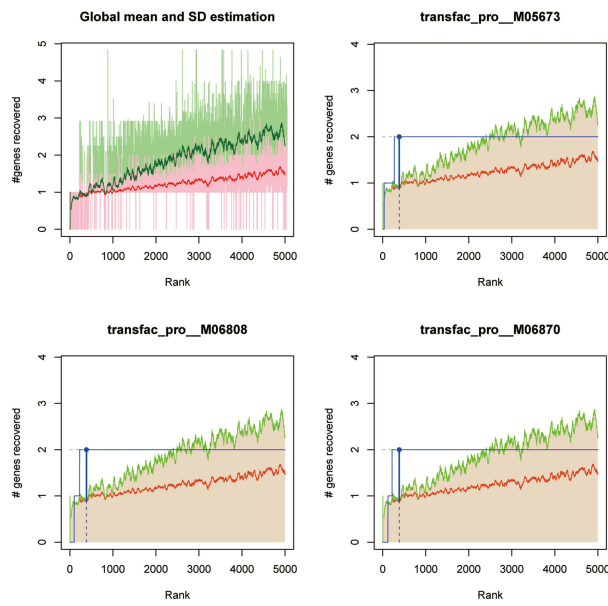


Figure 11 GSEA analysis of key genes. KEGG signaling pathway is involved in key genes, as well as pathway regulation and involved genes (A-F).

A



B

logo	geneSet	motif	NES	AUC	TF_highConf	nEnrGenes	enrichedGenes
	key_gene	transfac_pro_M05673	9.36	0.574	ZNF136 (directAnnotation).	2	Cd44;Zfp36
	key_gene	transfac_pro_M06808	9.25	0.568	ZNF131 (directAnnotation).	2	Cf11;Zfp36
	key_gene	transfac_pro_M06870	9.18	0.563	ZNF131 (inferredBy_Orthology).	2	Cf11;Zfp36
	key_gene	hdpi_RAB18	9.02	0.554	RAB18 (directAnnotation).	2	Cd44;Cf11
	key_gene	stark_SGGAAA	8.61	0.53	REL; RELA; RELB (inferredBy_Orthology).	2	Cd44;Cf11

C

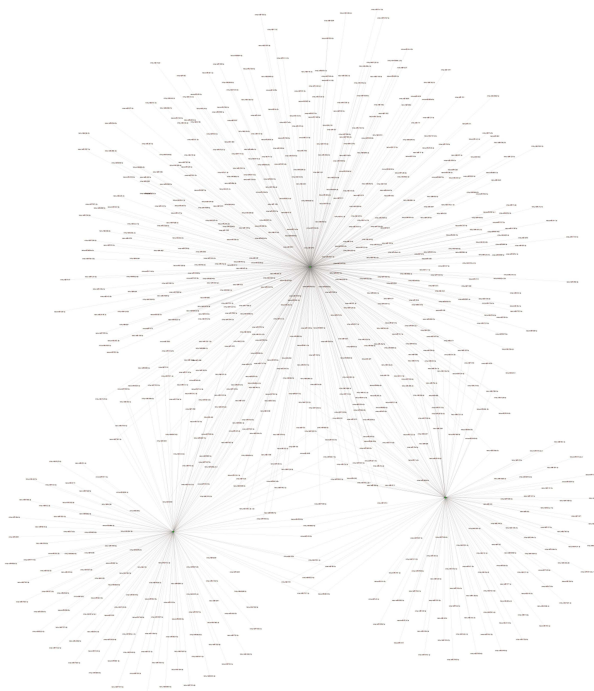


Figure 12 Key gene-related transcriptional regulation and miRNA network. **(A)** 4 motifs with higher AUC. The red line in the figure is the average recovery curve of each motif, the green line is the average + standard deviation, and the blue line is the current motif. Recovery curve. The maximum distance point between the current motif and the green curve (mean+sd). **(B)** All enriched motifs and corresponding transcription factors of key genes are displayed. **(C)** miRNA network of key genes, circles represent mRNA and inverted triangles represent miRNA.

Correlation Between miRNA Networks of Key Genes and Disease Regulatory Genes

This study utilized the targetscan database to identify non-coding RNA networks linked to three key genes, predicting 771 miRNAs and 903 relationship pairs visualized in Cytoscape (Figure 12C). Subsequently, the GeneCards database was employed to identify MIRI progression-related genes. The expression levels of the top 20 genes with relevance scores were investigated, revealing significant differences in inter-group gene expression. Notably, Ctnnb1, 1b, and 6 genes exhibited significant relevance (Figure 13A). Analysis revealed a notable trend of elevated expression in the MIRI group for the three related hub genes, with statistically significant differences (Figure 13B). Furthermore, correlation analysis indicated a strong positive correlation ($r = 0.835$) between Cd44 and IL1b, as well as a strong positive correlation ($r = 0.78$) between Zfp36 and IL6 (Figure 13C).

Establishment of the MIRI Model

The TTC staining results are presented in Figure 14A and B; the white area in the MIRI group was significantly larger than that in the SHAM group ($p < 0.05$). The markers of myocardial injury, CK-MB and LDH, were higher after myocardial ischemia than in the MIRI group (Figure 14C and D) ($P < 0.05$). Figure 14E shows the regular arrangement of myocardial fibers in the SHAM group, free of inflammatory cells. In contrast, the MIRI model group had a disordered myocardial structure, myocardial interstitial edema, and an evident infiltration of inflammatory cells. In contrast to the SHAM surgery group, the ST segment increased during ischemia but decreased after reperfusion (Figure 14F).

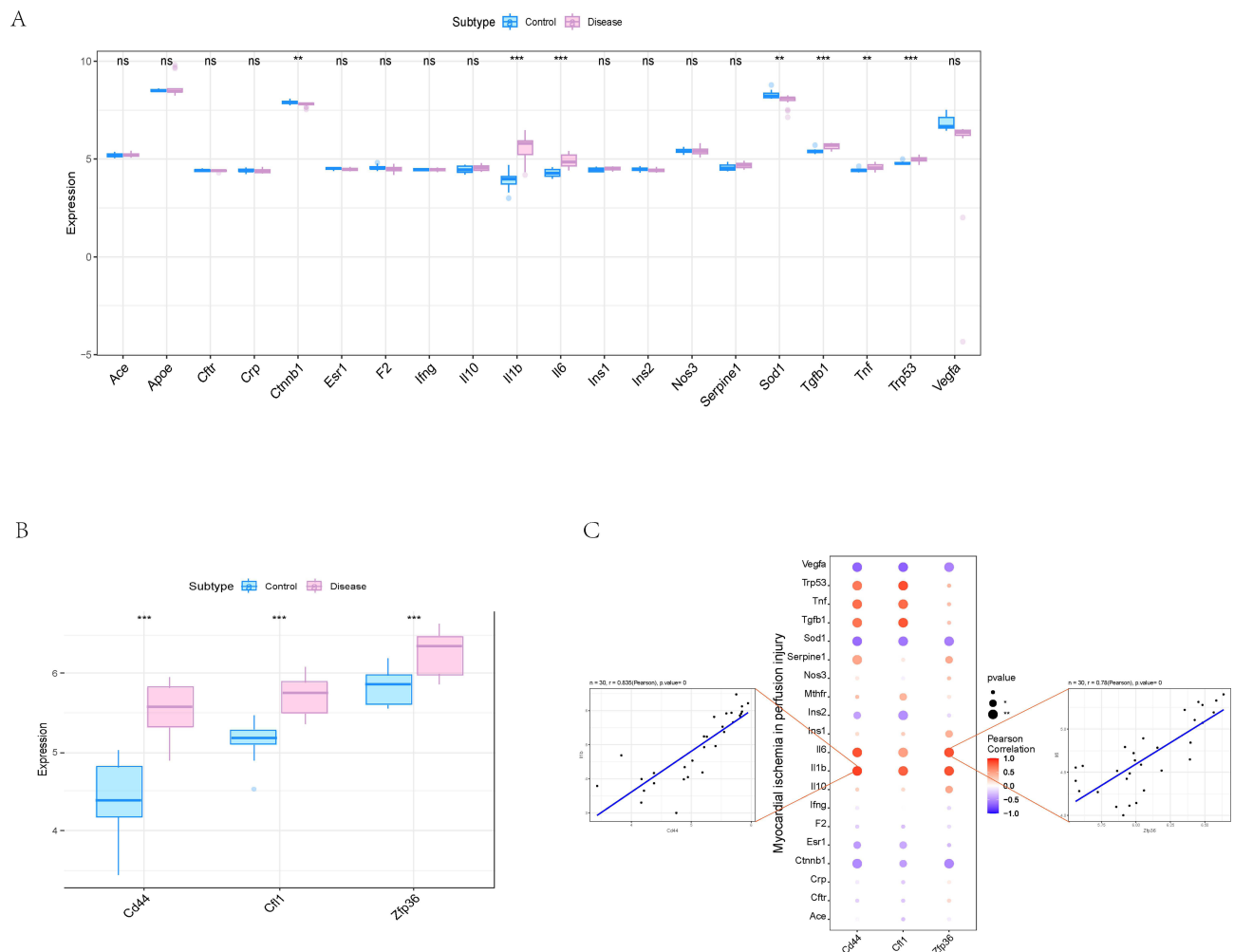


Figure 13 Correlation between key genes and disease progression genes and drug prediction. (A) Expression differences of disease regulatory genes. Blue indicates control patients and pink indicates disease patients. (B) Differences in expression of hub genes from the GEO database. Blue indicates the control group and pink indicates disease group. (C) Pearson correlation analysis of key genes and disease genes. Blue indicates a negative correlation and red indicates a positive correlation.

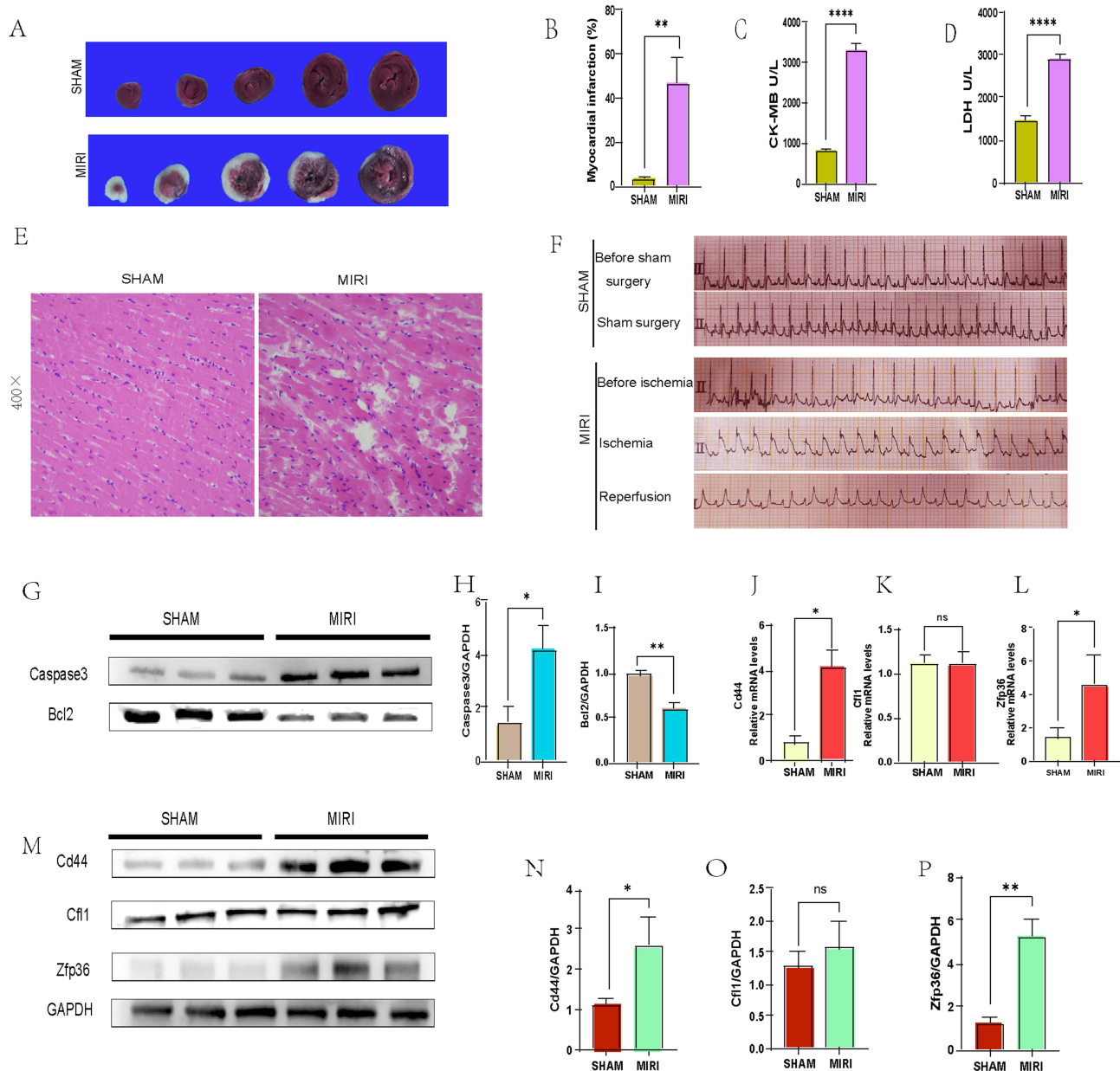


Figure 14 Construction of the MIRI model and verification of the expression levels of Cd44, Zfp36, and Cfl1. (A) TTC assay was performed to test the myocardial infarct size (B) The ratio of the myocardial infarction size to the total area of the section. (C) Serum CK-MB levels were detected by ELISA. (D) Serum LDH levels were detected by ELISA. (E) Results of HE staining ($\times 400$). (F) Electrocardiographic waveforms of infarction and reperfusion. (G and H) Protein expression and analysis of Caspase3, Bcl2 between the two groups. (I) RT-qPCR verified the difference in gene mRNA expression in rat myocardial tissue between the SHAM group and the MIRI group. (J and K) Protein expression and analysis of Cd44, Zfp36, Cfl1 and GAPDH between the two groups. * $P < 0.05$ vs SHAM group, ** $P < 0.01$ vs SHAM group, *** $P < 0.001$ vs SHAM group, **** $P < 0.0001$ vs SHAM group.

Subsequently, MIRI increased caspase-3 protein levels and decreased Bcl2 protein levels (Figure 14G and H). Therefore, the indices mentioned above successfully established the MIRI model in vivo.

Verification of the Expression Levels of Cd44, Zfp36, and Cfl1 Between the Two Groups

RT-qPCR and Western blot verification confirmed the consistency of Cd44 and Zfp36 with database results, whereas Cfl1 protein and mRNA levels exhibited no variation (Figure 14I–K).

Flow Chart

A flow chart (Figure 15) summarizes the steps and logic used in this study.

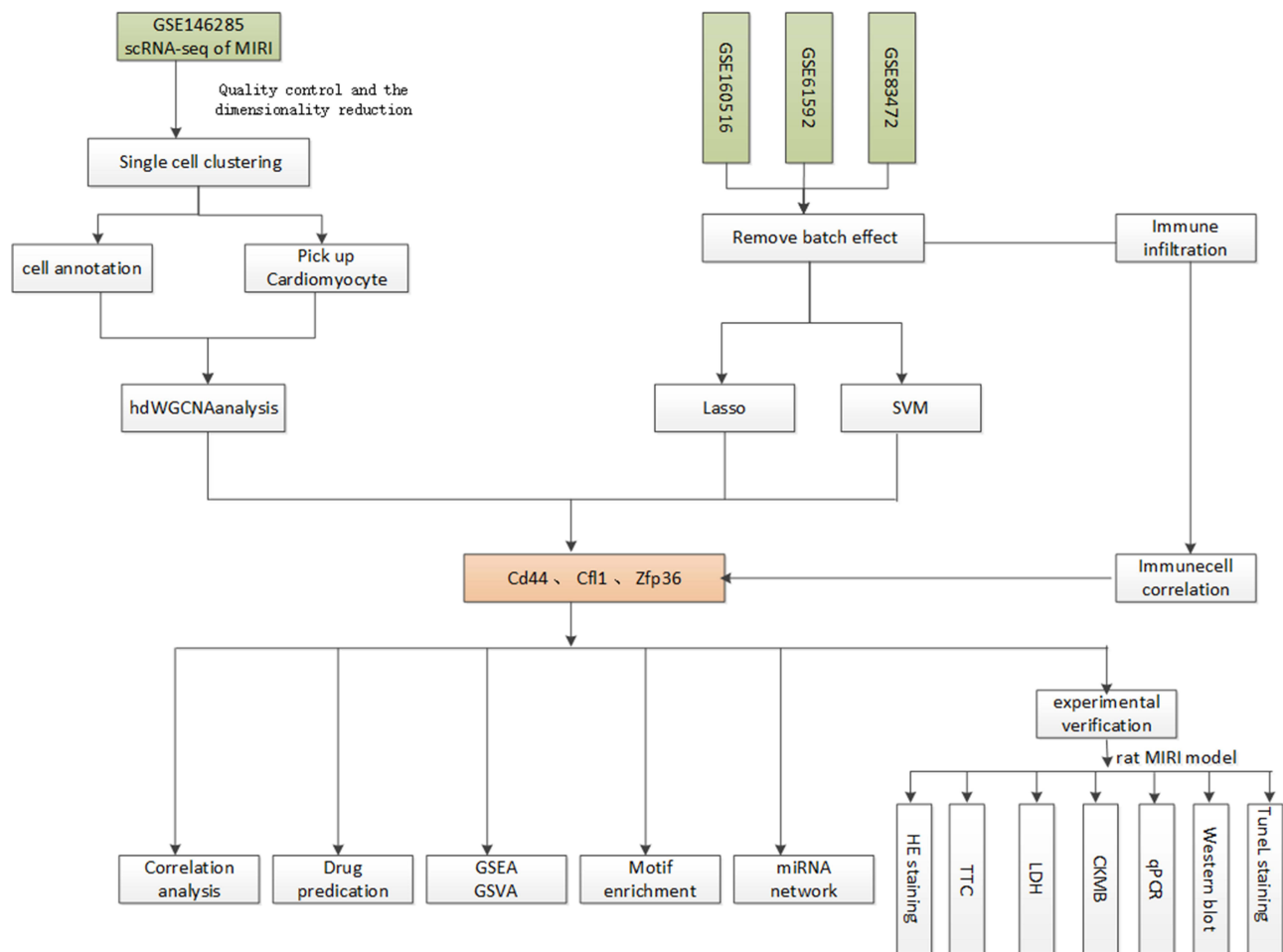


Figure 15 Flow chart of the study.

Discussion

Acute myocardial infarction is a leading cause of death globally.¹⁷ Coronary artery bypass grafting and direct percutaneous coronary intervention are practical techniques for recanalizing obstructed coronary arteries.^{2,18} However, these procedures frequently result in MIRI, causing acute and severe myocardial damage. MIRI is caused by oxidative stress, intracellular calcium overload, and inflammation, which increases myocardial cell death and lowers survival rates.¹⁹ MIRI's molecular mechanism is still unknown, so more research into MIRI-related genes is critical for identifying treatment and prevention targets.

While significant advances have been made in strategies for preventing or treating MIRI, there has been little research into the critical roles of immune cells in MIRI progression. During the early stages of MIRI, macrophages, a type of immune cell, are thought to play an essential regulatory function.^{20–22} T lymphocytes play a dual role in myocardial infarction, promoting wound healing and acting as a protective factor in the early stages²³ while contributing to left ventricular remodeling and progressive cardiac dysfunction in the later stages.²⁴ Eosinophils, mast cells, and basophils have been linked to coronary artery disease progression. Using bioinformatic methods to investigate the effect of immune-related genes on myocardial injury after obstructive coronary recanalization could provide helpful information. In this study, the levels of Eosinophil Cells, M0 Macrophage, M2 Macrophage, Mast Cells, Monocyte, T Cells CD4 Memory, T Cells CD8 Memory, and T Cells CD8 Naive in the MIRI group were significantly higher than in the control group, which was consistent with previous research findings.^{25–31} there was little research into the roles of DC Activated and DC Mature in MIRI. The exact regulatory mechanisms of these immune-infiltrating cells in MIRI remain unknown.

Reactive oxygen species (ROS) and lipid peroxidation distinguish ferroptosis, a newly discovered iron-dependent cell death mechanism. Inhibiting ferroptosis has been shown to improve MIRI.^{32–34} According to emerging evidence, ferroptosis will likely cause an inflammatory response that activates the innate immune system. These factors control inflammation, signal transduction, and cell proliferation. Ferroptosis is associated with the NOD-like receptor family pyrin domain-containing 3 (NLRP3) inflammasome, which is involved in inflammatory responses and aseptic injury.³⁵ As revealed by recent research, the NLRP3 inflammasome is critical for regulating MIRI through ferroptosis-mediated inflammation. Moreover, excess intracellular iron can activate the NLRP3 inflammasome, resulting in oxidative stress and ferroptosis via the cGAS-STING1 pathway.³⁶ As a crucial negative regulator of ferroptosis, GPX4, a critical negative regulator of ferroptosis, is knocked out in mice, resulting in NLRP3 inflammasome activation and pyroptosis.³⁷ Further research is needed to understand the pathogenesis of the ferroptosis-mediated inflammatory response in MIRI.

Cd44, a cell surface adhesion molecule, is widely expressed by various cell types, including tumor and endothelial cells. Despite its role in promoting angiogenesis in cancer, it also protects against ischemic diseases.³⁸ It is upregulated in myocardial infarction tissues, regulating inflammation, fibrosis, and angiogenesis following myocardial infarction.^{39,40} The high Cd44 expression in rat MIRI tissues as observed in this study aligns with previous research findings. Subsequently, RT-qPCR and Western blot confirmed the Cd44 expression levels.

A Pearson correlation analysis of key and disease-related genes reveals a strong relationship between CD44 and interleukin. The pro-inflammatory cytokine IL-1 β has been linked to the severity and progression of heart disease. In patients with myocardial infarction, targeted inhibition of the IL-1 signaling pathway may be a promising treatment strategy.^{41,42} Research has shown that IL-1 stimulation increases CD44 levels.^{43,44} Upregulation of CD44 levels may increase resistance to MIRI by targeting the key gene IL1 β , impacting ferroptosis and MIRI. GSEA analysis revealed that Cd44 was significantly upregulated in MIRI's IL6_JAK_STAT3_SIGNALING and IL2_STAT5_SIGNALING pathways. Therefore, Cd44, along with these two signaling pathways, is expected to play a critical role in MIRI. It was further discovered that upregulating IL6 influenced the expression of pro-inflammatory factors via Cd44, altered the extracellular matrix composition, and protected the myocardium during acute myocardial infarction.⁴⁵ The evidence on whether Cd44 regulates MIRI through the IL2_STAT5_SIGNALING signaling pathway is limited. Meanwhile, Cd44's role in ferroptosis is debatable. It was proposed in one study that Cd44 inhibits the exacerbation of ferroptosis in tumor diseases,⁴⁶ whereas other studies have found a positive correlation between the molecule and ferroptosis severity.^{47,48} The role of Cd44 in regulating ferroptosis in MIRI is unclear, highlighting the need for additional research in this area.

RT-qPCR and Western blot confirmed Zfp36 expression in rat samples. Zfp36 is known for its anti-inflammatory and anti-apoptotic properties, which help protect against lung and brain ischemia-reperfusion injuries.^{49,50} Previous bioinformatics studies have found varying levels of Zfp36 expression in neutrophils and endothelial cells in blood samples from people with acute myocardial infarction.^{51,52} Despite this, literature on Zfp36 expression and related molecular mechanisms in MIRI is scarce. The mechanisms of this molecule in MIRI need to be investigated further. It was discovered that overexpressing Zfp36 can suppress ferroptosis via the ATG16L1 pathway.⁵³ Furthermore, in neuronal tissue, Zfp36 was identified to have a negative regulatory impact on ferroptosis.⁵⁴ This study found a significant upregulation of Zfp36 in the MIRI group, indicating a potential compensatory mechanism to improve MIRI by suppressing ferroptosis. This upregulation may impact signaling pathways such as TGF_BETA_SIGNALING and MTORC1_SIGNALING.⁵⁵ Previous research has shown that increasing MTOR expression may mitigate MIRI. Additionally, one study identified MTOR as a ferroptosis suppressor.⁵⁶ Zfp36 is not only associated with immune cell infiltration but is also positively correlated with IL6 levels, suggesting that the immune microenvironment may play an essential role in Zfp36 regulation of MIRI. Nevertheless, additional experiments involving Zfp36 knockdown or overexpression in the MIRI model are required to observe changes in ferroptosis and myocardial injury.

Despite its findings, this study has some limitations. First, using a mouse model may limit the generalizability of the findings. Second, the sample size is limited; increasing it would improve the data's credibility. Finally, the role and detailed mechanism of genes such as Zfp36 in MIRI must be clarified through knockdown or overexpression studies investigating relevant mechanisms.

Conclusion

Two key genes, Zfp36 and Cd44, positively affected MIRI by influencing signal pathways, improving the immune microenvironment, and regulating ferroptosis. These findings indicate that targeting these genes may provide novel therapeutic approaches for MIRI mitigation.

Ethics Statement

The study was approved by the Research Ethics Committee of the Affiliated Hospital of Youjiang Medical College of Nationalities (ethics approval number: YYFY-LL-2024-029).

Acknowledgment

We extend our gratitude to the GEO database and its contributors for making the relevant datasets available for research purposes.

Funding

This study was funded by the National Natural Science Foundation of China, Grant No. 82260883.

Disclosure

The authors have no relevant financial or non-financial interests to disclose in this work.

References

1. Cho KH, Han X, Ahn JH. et al. Long-Term Outcomes of Patients With Late Presentation of ST-Segment Elevation Myocardial Infarction. *J Am Coll Cardiol.* 2021;77(15):1859–1870. doi:10.1016/j.jacc.2021.02.041
2. Hausenloy DJ, Yellon DM. Myocardial ischemia-reperfusion injury: a neglected therapeutic target. *J Clin Invest.* 2013;123(1):92–100. doi:10.1172/JCI62874
3. Roger VL, Go AS, Lloyd-Jones DM, et al. Heart disease and stroke statistics--2011 update: a report from the American Heart Association. *Circulation.* 2011;123(4):e18–e209. doi:10.1161/CIR.0b013e3182009701
4. Ibanez B, Heusch G, Ovize M, Van de Werf F. Evolving therapies for myocardial ischemia/reperfusion injury. *J Am Coll Cardiol.* 2015;65(14):1454–1471. doi:10.1016/j.jacc.2015.02.032
5. Bellanti F. Hypoxia-inducible factor-1 in myocardial ischaemia/reperfusion injury. *Acta Physiol.* 2017;221(2):93–94. doi:10.1111/apha.12903
6. Stockwell BR, Friedmann Angeli JP, Bayir H, et al. Ferroptosis: a Regulated Cell Death Nexus Linking Metabolism, Redox Biology, and Disease. *Cell.* 2017;171(2):273–285. doi:10.1016/j.cell.2017.09.021
7. Lv Z, Wang F, Zhang X, Zhang X, Zhang J, Liu R. Etomidate Attenuates the Ferroptosis in Myocardial Ischemia/Reperfusion Rat Model via Nrf2/HO-1 Pathway. *Shock.* 2021;56(3):440–449. doi:10.1097/SHK.0000000000001751
8. Xu X, Mao C, Zhang C, Zhang M, Gong J, Wang X. Salvianolic Acid B Inhibits Ferroptosis and Apoptosis during Myocardial Ischemia/Reperfusion Injury via Decreasing the Ubiquitin-Proteasome Degradation of GPX4 and the ROS-JNK/MAPK Pathways. *Molecules.* 2023;29(1):28. doi:10.3390/molecules28104117
9. Yin J, Zheng X, Zhao Y, et al. Investigating the Therapeutic Effects of Ferroptosis on Myocardial Ischemia-Reperfusion Injury Using a Dual-Locking Mitochondrial Targeting Strategy. *Angew Chem Int Ed Engl.* 2024;2024:e202402537. doi:10.1002/anie.202402537
10. Kolodziejczyk AA, Kim JK, Svensson V, Marioni JC, Teichmann SA. The technology and biology of single-cell RNA sequencing. *Mol Cell.* 2015;58(4):610–620. doi:10.1016/j.molcel.2015.04.005
11. Gawad C, Koh W, Quake SR. Single-cell genome sequencing: current state of the science. *Nat Rev Genet.* 2016;17(3):175–188. doi:10.1038/nrg.2015.16
12. Stuart T, Butler A, Hoffman P, et al. Comprehensive Integration of Single-Cell Data. *Cell.* 2019;177(7):1888–1902e21. doi:10.1016/j.cell.2019.05.031
13. Efremova M, Vento-Tormo M, Teichmann SA, Vento-Tormo R. CellPhoneDB: inferring cell-cell communication from combined expression of multi-subunit ligand-receptor complexes. *Nat Protoc.* 2020;15(4):1484–1506. doi:10.1038/s41596-020-0292-x
14. Langfelder P, Horvath S. WGCNA: an R package for weighted correlation network analysis. *BMC Bioinf.* 2008;9(1):559. doi:10.1186/1471-2105-9-559
15. Friedman J, Hastie T, Tibshirani R. Regularization Paths for Generalized Linear Models via Coordinate Descent. *J Stat Softw.* 2010;33(1):1–22. doi:10.18637/jss.v033.i01
16. Newman AM, Liu CL, Green MR, et al. Robust enumeration of cell subsets from tissue expression profiles. *Nat Methods.* 2015;12(5):453–457. doi:10.1038/nmeth.3337
17. Tsao CW, Aday AW, Almarzoq ZI, et al. Heart Disease and Stroke Statistics-2022 Update: a Report From the American Heart Association. *Circulation.* 2022;145(8):e153–e639. doi:10.1161/CIR.0000000000001052
18. Piao H, Takahashi K, Yamaguchi Y, Wang C, Liu K, Naruse K. Transient receptor potential melastatin-4 is involved in hypoxia-reoxygenation injury in the cardiomyocytes. *PLoS One.* 2015;10(4):e0121703. doi:10.1371/journal.pone.0121703
19. Kalogeris T, Baines CP, Krenz M, Korthuis RJ. Ischemia/Reperfusion. *Compr Physiol.* 2016;7:113–170. doi:10.1002/cphy.c160006

20. Yue Y, Yang X, Feng K, et al. M2b macrophages reduce early reperfusion injury after myocardial ischemia in mice: a predominant role of inhibiting apoptosis via A20. *Int J Cardiol.* 2017;245:228–235. doi:10.1016/j.ijcard.2017.07.085
21. Cao Y, Xu Y, Auchoybur ML, et al. Regulatory role of IKKa in myocardial ischemia/reperfusion injury by the determination of M1 versus M2 polarization of macrophages. *J Mol Cell Cardiol.* 2018;123:1–12. doi:10.1016/j.yjmcc.2018.08.021
22. Ben-Mordechai T, Holbova R, Landa-Rouben N, et al. Macrophage subpopulations are essential for infarct repair with and without stem cell therapy. *J Am Coll Cardiol.* 2013;62(20):1890–1901. doi:10.1016/j.jacc.2013.07.057
23. Hofmann U, Beyersdorf N, Weirather J, et al. Activation of CD4 + T Lymphocytes Improves Wound Healing and Survival After Experimental Myocardial Infarction in Mice. *Circulation.* 2012;125(13):1652–1663. doi:10.1161/CIRCULATIONAHA.111.044164
24. Kumar V, Prabhu SD, Bansal SS. CD4(+) T-lymphocytes exhibit biphasic kinetics post-myocardial infarction. *Front Cardiovasc Med.* 2022;9:992653. doi:10.3389/fcvm.2022.992653
25. Liu J, Yang C, Liu T, et al. Eosinophils improve cardiac function after myocardial infarction. *Nat Commun.* 2020;11(1):6396. doi:10.1038/s41467-020-19297-5
26. Ryabov V, Gombozhapova A, Rogovskaya Y, Kzhyshkowska J, Rebenkova M, Karpov R. Cardiac CD68+ and stabilin-1+ macrophages in wound healing following myocardial infarction: from experiment to clinic. *Immunobiology.* 2018;223(4–5):413–421. doi:10.1016/j.imbio.2017.11.006
27. Jung K, Kim P, Leuschner F, et al. Endoscopic time-lapse imaging of immune cells in infarcted mouse hearts. *Circ Res.* 2013;112(6):891–899. doi:10.1161/CIRCRESAHA.111.300484
28. Lee WW, Marinelli B, van der Laan AM, et al. PET/MRI of inflammation in myocardial infarction. *J Am Coll Cardiol.* 2012;59(2):153–163. doi:10.1016/j.jacc.2011.08.066
29. Kupreishvili K, Fuijkschot WW, Vonk AB, et al. Mast cells are increased in the media of coronary lesions in patients with myocardial infarction and may favor atherosclerotic plaque instability. *J Cardiol.* 2017;69(3):548–554. doi:10.1016/j.jcc.2016.04.018
30. Yan X, Anzai A, Katsumata Y, et al. Temporal dynamics of cardiac immune cell accumulation following acute myocardial infarction. *J Mol Cell Cardiol.* 2013;62:24–35. doi:10.1016/j.yjmcc.2013.04.023
31. Curato C, Slavic S, Dong J, et al. Identification of noncytotoxic and IL-10-producing CD8+AT2R+ T cell population in response to ischemic heart injury. *J Immunol.* 2010;185(10):6286–6293. doi:10.4049/jimmunol.0903681
32. Cai W, Liu L, Shi X, et al. Alox15/15-HpETE Aggravates Myocardial Ischemia-Reperfusion Injury by Promoting Cardiomyocyte Ferroptosis. *Circulation.* 2023;147(19):1444–1460. doi:10.1161/CIRCULATIONAHA.122.060257
33. Yan J, Li Z, Liang Y, et al. Fucoxanthin alleviated myocardial ischemia and reperfusion injury through inhibition of ferroptosis via the NRF2 signaling pathway. *Food Funct.* 2023;14(22):10052–10068. doi:10.1039/d3fo02633g
34. Qian W, Liu D, Han Y, et al. Cyclosporine A-loaded apoferritin alleviates myocardial ischemia-reperfusion injury by simultaneously blocking ferroptosis and apoptosis of cardiomyocytes. *Acta Biomater.* 2023;160:265–280. doi:10.1016/j.actbio.2023.02.025
35. Toldo S, Mauro AG, Cutter Z, Abbate A. Inflammasome, pyroptosis, and cytokines in myocardial ischemia-reperfusion injury. *Am J Physiol Heart Circ Physiol.* 2018;315:H1553–H1568. doi:10.1152/ajpheart.00158.2018
36. Gupta U, Ghosh S, Wallace CT, et al. Increased LCN2 (lipocalin 2) in the RPE decreases autophagy and activates inflammasome-ferroptosis processes in a mouse model of dry AMD. *Autophagy.* 2023;19(1):92–111. doi:10.1080/15548627.2022.2062887
37. Kang R, Zeng L, Zhu S, et al. Lipid Peroxidation Drives Gasdermin D-Mediated Pyroptosis in Lethal Polymicrobial Sepsis. *Cell Host Microbe.* 2018;24(1):97–108e4. doi:10.1016/j.chom.2018.05.009
38. Chen L, Fu C, Zhang Q, He C, Zhang F, Wei Q. The role of CD44 in pathological angiogenesis. *FASEB J.* 2020;34(10):13125–13139. doi:10.1096/fj.202000380RR
39. Huebener P, Abou-Khamis T, Zymek P, et al. CD44 is critically involved in infarct healing by regulating the inflammatory and fibrotic response. *J Immunol.* 2008;180(4):2625–2633. doi:10.4049/jimmunol.180.4.2625
40. Zhang Q, Chen L, Huang L, et al. CD44 promotes angiogenesis in myocardial infarction through regulating plasma exosome uptake and further enhancing FGFR2 signaling transduction. *Mol Med.* 2022;28(1):145. doi:10.1186/s10020-022-00575-5
41. Saxena A, Russo I, Frangiannnis NG. Inflammation as a therapeutic target in myocardial infarction: learning from past failures to meet future challenges. *Transl Res.* 2016;167(1):152–166. doi:10.1016/j.trsl.2015.07.002
42. Evans HG, Lewis MJ, Shah AM. Interleukin-1 beta modulates myocardial contraction via dexamethasone sensitive production of nitric oxide. *Cardiovasc Res.* 1993;27(8):1486–1490. doi:10.1093/cvr/27.8.1486
43. Ferreira JR, Caldeira J, Sousa M, et al. Dynamics of CD44(+) bovine nucleus pulposus cells with inflammation. *Sci Rep.* 2024;14(1):9156. doi:10.1038/s41598-024-59504-7
44. Govindaraju P, Todd L, Shetye S, Monslow J, Pure E. CD44-dependent inflammation, fibrogenesis, and collagenolysis regulates extracellular matrix remodeling and tensile strength during cutaneous wound healing. *Matrix Biol.* 2019;75–76:314–330. doi:10.1016/j.matbio.2018.06.004
45. Muller J, Gorressen S, Grandoch M, et al. Interleukin-6-dependent phenotypic modulation of cardiac fibroblasts after acute myocardial infarction. *Basic Res Cardiol.* 2014;109(6):440. doi:10.1007/s00395-014-0440-y
46. Liu T, Jiang L, Tavana O, Gu W. The Deubiquitylase OTUB1 Mediates Ferroptosis via Stabilization of SLC7A11. *Cancer Res.* 2019;79(8):1913–1924. doi:10.1158/0008-5472.CAN-18-3037
47. Lei G, Zhuang L, Gan B. Targeting ferroptosis as a vulnerability in cancer. *Nat Rev Cancer.* 2022;22(7):381–396. doi:10.1038/s41568-022-00459-0
48. Muller S, Sindikubwabo F, Caneque T, et al. CD44 regulates epigenetic plasticity by mediating iron endocytosis. *Nat Chem.* 2020;12(10):929–938. doi:10.1038/s41557-020-0513-5
49. Cao Y, Huang W, Wu F, et al. ZFP36 protects lungs from intestinal I/R-induced injury and fibrosis through the CREBBP/p53/p21/Bax pathway. *Cell Death Dis.* 2021;12(7):685. doi:10.1038/s41419-021-03950-y
50. Guo H, Jiang Y, Gu Z, et al. ZFP36 protects against oxygen-glucose deprivation/reoxygenation-induced mitochondrial fragmentation and neuronal apoptosis through inhibiting NOX4-DRP1 pathway. *Brain Res Bull.* 2022;179:57–67. doi:10.1016/j.brainresbull.2021.12.003
51. Xiang J, Shen J, Zhang L, Tang B. Identification and validation of senescence-related genes in circulating endothelial cells of patients with acute myocardial infarction. *Front Cardiovasc Med.* 2022;9:1057985. doi:10.3389/fcvm.2022.1057985
52. Ke D, Ni J, Yuan Y, Cao M, Chen S, Zhou H. Identification and Validation of Hub Genes Related to Neutrophil Extracellular Traps-Mediated Cell Damage During Myocardial Infarction. *J Inflamm Res.* 2024;17:617–637. doi:10.2147/JIR.S444975

53. Zhang Z, Guo M, Li Y, et al. RNA-binding protein ZFP36/TTP protects against ferroptosis by regulating autophagy signaling pathway in hepatic stellate cells. *Autophagy*. 2020;16(8):1482–1505. doi:10.1080/15548627.2019.1687985
54. Yu X, Yang Y, Zhang B, et al. Ketone Body beta-Hydroxybutyric Acid Ameliorates Dopaminergic Neuron Injury Through Modulating Zinc Finger Protein 36/Acyl-CoA Synthetase Long-Chain Family Member Four Signaling Axis-Mediated Ferroptosis. *Neuroscience*. 2023;509:157–172. doi:10.1016/j.neuroscience.2022.11.018
55. Xiao Y, Chen W, Zhong Z, et al. Electroacupuncture preconditioning attenuates myocardial ischemia-reperfusion injury by inhibiting mitophagy mediated by the mTORC1-ULK1-FUNDC1 pathway. *Biomed Pharmacother*. 2020;127:110148. doi:10.1016/j.biopha.2020.110148
56. Baba Y, Higa JK, Shimada BK, et al. Protective effects of the mechanistic target of rapamycin against excess iron and ferroptosis in cardiomyocytes. *Am J Physiol Heart Circ Physiol*. 2018;314:H659–H668. doi:10.1152/ajpheart.00452.2017.

Journal of Inflammation Research

Dovepress

Publish your work in this journal

The Journal of Inflammation Research is an international, peer-reviewed open-access journal that welcomes laboratory and clinical findings on the molecular basis, cell biology and pharmacology of inflammation including original research, reviews, symposium reports, hypothesis formation and commentaries on: acute/chronic inflammation; mediators of inflammation; cellular processes; molecular mechanisms; pharmacology and novel anti-inflammatory drugs; clinical conditions involving inflammation. The manuscript management system is completely online and includes a very quick and fair peer-review system. Visit <http://www.dovepress.com/testimonials.php> to read real quotes from published authors.

Submit your manuscript here: <https://www.dovepress.com/journal-of-inflammation-research-journal>